EPRI | ELECTRIC POWER RESEARCH INSTITUTE

Development of Multiplexed Fiber-Optic Sensors for On-line Monitoring of Electrical Faults and Thermal Faults Inside High Voltage Transformers

1012342

Development of Multiplexed Fiber-Optic Sensors for On-line Monitoring of Electrical Faults and Thermal Faults Inside High Voltage Transformers

1012342

Technical Update, December 2006

EPRI Project Manager
L. Van der Zel

ELECTRIC POWER RESEARCH INSTITUTE
3420 Hillview Avenue, Palo Alto, California 94304-1338 ▪ PO Box 10412, Palo Alto, California 94303-0813 ▪ USA
800.313.3774 ▪ 650.855.2121 ▪ askepri@epri.com ▪ www.epri.com

DISCLAIMER OF WARRANTIES AND LIMITATION OF LIABILITIES

ORGANIZATION(S) THAT PREPARED THIS DOCUMENT

Virginia Polytechnic Institute and State University

NOTE

For further information about EPRI, call the EPRI Customer Assistance Center at 800.313.3774 or e-mail askepri@epri.com.

CITATIONS

This report was prepared by

Virginia Polytechnic Institute and State University
Bradley Department of Electrical and Computer Engineering
Blacksburg, VA 24061-0111

Principal Investigator
A. Wang

This report describes research sponsored by the Electric Power Research Institute (EPRI).

This publication is a corporate document that should be cited in the literature in the following manner:

Development of Multiplexed Fiber-Optic Sensors for On-line Monitoring of Electrical Faults and Thermal Faults Inside High Voltage Transformers. EPRI, Palo Alto, CA: 2006. 1012342.

REPORT SUMMARY

Background

High voltage transformers represent one of the most important and expensive devices in the power industry. In the high voltage transformers, a decisive significance is attributed to a secure and permanent insulation. However, under operating conditions the electrical, thermal and mechanical aging affects the insulating medium inside high voltage transformers. Electrical faults such as Partial Discharges (PD's) and thermal faults (hot spots) occurring within transformers may lead to insulation breakdown and catastrophic failures. Impacts may be large in both safety and financial terms. The cost of each failure can easily drive the total cost of a large transformer failure into more than ten million dollars.

Hence, it is important that the partial discharge activities and thermal faults be monitored and studied to detect incipient insulation problems, to prevent catastrophic failures, and to prevent extensive costs. A variety of physical-chemical diagnostic methods have been developed and introduced into regular use to determine the state of power transformers. One of these methods is Dissolved Gas Analysis (DGA), conducted from samples of transformer oil or on-line during normal operation of the power transformer.

Fiber optic sensors have been demonstrated for the detection of a large variety of physical and chemical parameters, including partial discharges and temperature inside a high voltage transformer. The advantages of using fiber optic sensors are that fiber optic sensors are intrinsically immune to electromagnetic interference, light and compact in size and therefore can be placed inside the transformer tank without affecting the insulation integrity. By placing sensors inside the transformer tank, point measurement of temperature can be achieved, and PD detection and location accuracy can be significantly improved because of the reduced attenuation and multi-path effects of PD generated acoustic waves. What is more important is that fiber optic sensors have the great potential of multiplexing which means distributed electrical and thermal faults detection can be achieved with a single signal conditioner. This multiplexing capability may significantly reduce the system design complexity and cost.

Sponsored by EPRI from 1999 to 2003, the Center for Photonics Technology (CPT) at Virginia Tech has developed a diaphragm-based fiber Fabry-Perot sensor technology for the on-line detection of the acoustic waves generated by PD's inside high voltage power transformers. Laboratory experiments at CPT, a field tests on the Northfleet STG3A 400/275KV transformer of National Grid (UK), and two tests with simulated power transformer setup at J. W. Harley, Inc in Twingsburg and the Transformer Lab of Rensselaer Polytechnic Institute indicate that the developed fiber optic acoustic sensors are capable of detecting both electrical and thermal activities in transformer oil with a large sensitivity range and a wide bandwidth from 20kHz to

300kHz. Directly based on this research, we develop a multiplexed PD detection system that can monitor the PD activities at multipoint inside a transformer. Furthermore, we will incorporate multipoint temperature measurement for hot-spot detection into this system.

Objectives

The objective of the research is to develop an integrated fiber optic sensor system with multiplexed PD sensors and temperature sensors for the on-line detection of electrical faults and thermal faults at multiple points inside a high voltage transformer.

Approach

The integrated fiber optic sensor system can be divided into two sub-systems. The first is the multipoint temperature measurement sub-system which is achieved by wavelength division multiplexed fiber Bragg gratings. The second is the PD detection subsystem which is achieved by diaphragm-based extrinsic Fabry-Perot interferometric fiber optic sensors. The PD sensors are multiplexed through a star topology.

Results

A bench-top fiber optic sensor system for on-line monitoring of hot-spots and PD activities is built and demonstrated at laboratory. Nine temperature sensors and four PD sensors are multiplexed in the system. The temperature measurement resolution is better than 0.1 °C for each temperature sensors and the PD sensors are demonstrated to have a better sensitivity to PD generated acoustic waves compared to external sensors on the tank wall. Research has been completed to solve the challenge of detecting acoustic waves at varying background hydrostatic pressures.

Keywords

Hot-spot measurements
Partial Discharge Detection
Transformers
Fiber Optic Sensors
Multiplexing

CONTENTS

1 **INTRODUCTION 1-1**

1.1 Research Background 1-1

1.2 Previous work 1-2

1.3 Technical Approach 1-4

2 **TEMPERATUE SENSORS 2-1**

2.1 Principle of Operation 2-1

2.2 Sensor Fabrication 2-3

Hydrogen Loading System 2-3

FBG Fabrication System 2-4

Sensor Annealing 2-7

2.3 Signal Processing 2-8

2.4 Temperature Sensor Test 2-8

Sensor Responsivity 2-8

Sensor Stability 2-9

Measurement Resolution 2-10

3 **PARTIAL-DISCHARGE SENSORS 3-1**

3.1 Principle of Operation 3-1

3.2 Two-wavelength Quadrature Demodulation 3-3

3.3 Sensor Structure and Fabrication 3-6

3.4 Optical Receiver Circuits 3-9

3.5 Single Channel PD Detection 3-11

4 **SYSTEM IMPLEMENTATION 4-1**

4.1 Schematic of the Entire System 4-1

4.2 Bench-top Demonstration System 4-2

4.3 Comparison with Electronic Acoustic Sensors 4-4

Test 1: Optical Sensor Inside Tank and PZT Sensor Outside Tank 4-4
Test 2: Reflection Loss due to Tank Wall 4-6
Test 3: Head-to-Head Comparison of Optical and PZT Sensor Systems 4-7

5 **CONCLUSIONS 5-1**

6 **SUGGESTION FOR FUTURE WORK 6-1**

LIST OF FIGURES

Figure 1-1 Principle Diagram of the Diaphragm-Based Fiber Optic PD Sensor System 1-3

Figure 1-2 Schematic of the Technical Approach Used in the Research..... 1-5

Figure 1-3 Effect View of the Portable and Field-Test-Ready Instrumentation System – which is proposed for development in 2007. 1-5

Figure 2-1 Schematic of a Fiber-Bragg-Grating (a); and Its Reflection Spectrum (b) 2-1

Figure 2-2 Wavelength Division Multiplexing of Fiber Bragg Grating Sensors; CTS, Component Test System..... 2-2

Figure 2-3 Hydrogen-Loading System 2-4

Figure 2-4 Schematic of the Phase Mask Interferometer for FBG Sensor Fabrication..... 2-5

Figure 2-5 A Photograph of the Tunable Phase Mask Interferometer 2-5

Figure 2-6 Reflection Spectrum of Nine FBG sensors Fabricated In a Single Span of Fiber; (a) In Logarithmic Scale and (b) In Linear Scale..... 2-6

Figure 2-7 Bragg Wavelength Shift during Annealing..... 2-7

Figure 2-8 Responsivity Test of the Nine Temperature Sensors; (a) Bragg Wavelength Shift versus Temperature Change; (b) Bar Chart of Responsivity Test Results 2-9

Figure 2-9 Fluctuation of Bragg Wavelengths of FBG Sensors at 40°C over 24 Hours 2-10

Figure 2-10 Bar Chart of Measurement Resolution of FBG Sensors..... 2-10

Figure 3-1 Schematic of the Diaphragm-Based PD Sensor Head..... 3-1

Figure 3-2 Two-laser quadrature detection (d~d') (a) the best condition; (b) the worst condition..... 3-4

Figure 3-3 Tow-laser quadrature detection (d>d') (a) the worst condition without background pressure; (b) the worst condition with background pressure. 3-5

Figure 3-4 Sensor Head Structure and Bonding (a) Schematic of Sensor Head; (b) Cross-Section View of the Sensor Head After Laser And Sol-Gel Bonging..... 3-7

Figure 3-5 Sensitivity and Resonant Frequency vs. Diaphragm Thickness..... 3-8

Figure 3-6 PD FP sensor fabrication (a) sensor fabrication setup; (b) close up picture of a PD FP sensor. 3-9

Figure 3-7 Reflection spectrum of a PD FP sensor in (a) transformer oil; (b) water 3-9

Figure 3-8 Optical Receiver Circuit. 3-10

Figure 3-9 (a) Optical Receiver Frequency Response; (b) Assembled 8-route Optical Receivers 3-10

Figure 3-10 Schematic of Single Channel PD Detection 3-11

Figure 3-11 Picture of the Single Channel PD Sensor Test System..... 3-11

Figure 3-12 Spectra and Output Signal from a PD Sensor in Three Conditions..... 3-12

Figure 4-1 Schematic of the Bench-Top System 4-1
Figure 4-2 PD Detection Module 4-2
Figure 4-3 Picture of Bench-top System 4-3
Figure 4-4 Relative Positions of the PD Source, Optical Sensor and PZT Sensor 4-4
Figure 4-5 Amplified Signals from the Optical Sensor and PZT Sensor 4-5
Figure 4-6 A Signals and Noises from (a) Optical Sensor and (b) PZT 4-6
Figure 4-7 Sensor Amplified Signals PZT Sensor (a) Inside Tank; (b) Outside Tank 4-7
Figure 4-8 Output Signal of the PZT and Optical Sensors When They Are Placed at the Same Position in the Transformer 4-8

1
INTRODUCTION

1.1 Research Background

High voltage transformers are one of the most important and expensive devices in the power industry. In the high voltage transformers, a decisive significance is attributed to a secure and permanent insulation. However, the inevitable and numerous mechanical, thermal, and electrical stresses these transformers undergo during their entire life of service often give rise to a degradation of the insulation systems. Thermal faults (hot-spots) and electrical faults (partial-discharges or PD's) are the two major mechanisms that can lead to premature insulation breakdown and catastrophic transformer failures. The consequence of an unexpected transformer failure or outage can be dire in both safety and financial terms. A single transformer failure can easily drive the total cost into more than 10 million dollars. Therefore research is important in the detection of hot-spots and partial discharge activities to detect incipient insulation problems - so that remedial action can be taken to prevent catastrophic failures.

Hot-spots inside a transformer can be generated by either over-loading at peak usage period or local overheating occurring due to reduced cooling efficiency. Hot-spots put transformers into danger by accelerating the aging process of the insulation oils inside the transformer. According to a thermal-aging model, known as the Motzinger equation, the thermal aging rate doubles with every 6 °C rise of the hot-spots temperature above a temperature of 98 °C. [1] Thermal models that can determine the aging behavior and life expectance of the insulation have been presented by the IEEE Standard.[2] Alternative thermal models using the Motzinger equations are also under development by research institutes in corporation with industries. By monitoring the hot-spot temperatures, the estimate of the transformer life can be derived.

Partial Discharges and sparking internal to a transformer represents an undesirable situation that can further degrade the insulation over time – possibly leading to complete insulation failure and a resulting failure of the transformer. Partial Discharge and sparking detection is thus one of the useful parameters to measure in a transformer to help predict future insulation breakdown.

A variety of physical-chemical diagnostic methods have been developed and introduced into regular use to determine the state of power transformers. One of these methods is Dissolved Gas Analysis (DGA) which make use of the fact that gas is generated when an electrical arc or overheating develops inside the transformer. In this method sampling of transformer oil as well

[1] G, Betta and A. Pietrosanto, "An Enhanced Fiber-Optic Temperature Sensor System for Power Transformer Monitoring", IEEE Trans. Instr. Meas.
[2] "IEEE guide for loading mineral-oil-immersed power transformer rated in excess of 100 MVA (65°C)," IEEE/ANSI C.57.115.1991

as the gas analysis can be carried out during the operation of the transformer. Another category of methods is to monitor the temperatures and/or the partial discharge on line with different built-in sensors directly in the transformers – and these measurements are the focus of this report.

Partial discharges generate ultrasonic waves that are transmitted throughout the transformer via the oil medium, which provides an effective means for on-line partial discharge monitoring. Partial discharges have been detected using piezoelectric acoustic sensors. These sensors have most commonly been mounted on the outside wall of the transformers. There are several limitations for the outside-mounted acoustic sensors. First, the intensity of the acoustic waves that transmit to the sensors can be significantly reduced through the reflection on the transformer wall. It is reported that as much as 90% of the acoustic wave can be reflected by the transformer wall (corresponding to 20 dB loss of the acoustic wave).[3] An external sensor must have a much higher sensitivity than an internal one to detect a weak partial discharge activity. Secondly, the localization of the partial discharge is more difficult for the outside-mounted sensors. The localization is usually achieved by means of triangulation based on the times of propagation measured at the different positions of the sensors. The accuracy of this method is impacted by the fact that the ultrasonic wave travels to these sensors from the origin of the discharge along different paths and at different speeds – hence the research into possible internal measurements of PD.

The difficulties caused by the Electromagnetic Interference (EMI) in both temperature and partial discharge detections in high-voltage transformers can be eliminated when fiber-optic sensors are used. Fiber-optic sensors made from dielectric materials such as fused-silica glass and sapphire are inherently immune to the EMI. Many fiber-optic sensors have been developed for temperature and acoustic measurement. These sensors also possess the advantages of small size, light weight, and high sensitivity. Therefore they can be placed inside the transformer tank without affecting the performance of the sensors and the insulation integrity of the transformers. This is of great importance as for both the hot-spots and partial discharge detections. The approximation of the hot-spot temperature is more accurate when the temperature measurement is carried out closer to the winding; the partial discharge detection is more sensitive as much stronger ultrasonic waves are present inside the transformer. Moreover, fiber-optic sensors have the great potential of multiplexing which means that distributed electrical and thermal fault detection can be achieved with a single signal conditioner, providing the temperature profile of the winding and enabling the localization of the partial discharge origin. Furthermore, the multiplexing capability may significantly reduce the system design complexity and cost.

1.2 Previous work

Sponsored by the Electric Power Research Institute (EPRI) from 1999 to 2003, the Center for Photonics Technology (CPT) at Virginia Tech has developed a diaphragm-based extrinsic Fabry-Perot (FP) interferometric sensor technology for on-line detection of the acoustic waves generated by partial discharges inside high-voltage transformers. The principle diagram of the developed fiber optic PD sensor is shown in Figure 1-1. The sensor head consists of a FP cavity

[3] R. Meunier, G. H. Vaillancourt, "Propagation behaviour of acoustic partial discharge signals in oil-filled transformers," 12th International Conference on Conduction and Breakdown in Dielectric Liquids, Roma, Italy,1996

formed by the end of a single-mode fiber and the inner surface of a fused-silica diaphragm. The alignment between the fiber and the diaphragm is facilitated by the fused-silica ferrule and sleeve. The fiber, ferrule, sleeve, and diaphragm are bonded together by melting the borosilicate powder that is placed at the intended bonding points. The acoustic waves cause the vibration of the diaphragm, and consequently the vibration of the cavity length. Therefore by measuring the FP cavity length, the PD-generated acoustic wave can be detected. During the sensor operation, a fiber-optic circulator is used to direct the light from a superluminescent emitting diode (SLED) into the sensor head and the reflected signal from the sensor head into the photodetector. The interference between the reflections of the two FP cavity surfaces produces sinusoidal intensity variations, referred to as interference fringes, as the cavity length continuously changes. A tunable optical filter is used to select the appropriate operation wavelength for a specific FP cavity length which can drift during the operation due to temperature or background static pressure changes.

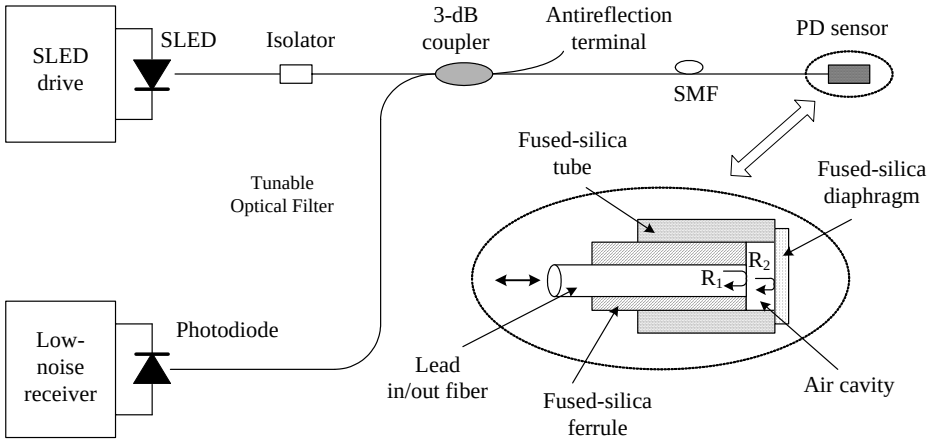

Figure 1-1
Principle Diagram of the Diaphragm-Based Fiber Optic PD Sensor System

Laboratory experiments at CPT, a field tests on the Northfleet STG3A 400/275KV transformer of National Grid (UK), and two tests with simulated power transformer setup at J. W. Harley, Inc in Twingsburg and the Transformer Lab of Rensselaer Polytechnic Institute indicate that the developed fiber optic acoustic sensors are capable of detecting the partial discharge activities in transformer oil with a large sensitivity range and a wide bandwidth from 20 to 300 kHz. In fact, CPT was one of the only two teams, out of the six teams attending the UK field test, who were able to observe the very weak partial discharge activities of the transformer. The feasibility of PD location has also been demonstrated at CPT with an accuracy of 1.0 cm.

Despite the great success we have achieved in the previous work, there are several limitations:

- The previous work at CPT was mainly focusing on the development of the sensor system for PD detection; while as discussed previously, both PD detection and hot-spot temperature monitoring are desirable for a more accurate diagnosis of the transformers
- The developed sensor system in the previous work can only carry out the PD detection at a single point. However, several PD sensors placed at different places of the transformer will

give a better chance to diagnose the PD at its early stage when the discharge level is still small. Moreover, multi-point PD detection is required for the localization of the PD origin. A multiplexed PD detection system would provide this multi-point PD detection with minimum cost.

- In the previous work, the fused-silica glass components of the sensor head were bonded together using the borosilicate inter-medium that is melted by a heating coil. The fabrication was not a trivial task involving the manipulation of the borosilicate powder on the tiny area of the glass tubes. The maximum operation temperature of the sensor head is limited by the softening point of the borosilicate powder which is 850 °C, much smaller than the fuse-silica. Moreover, the accurate control of the cavity length is difficult.
- In order to compensate the working point drift of the sensor head in the previous PD sensor system, the signal demodulation used a broadband light source (SLED) and a tunable optical filter. The bandwidth of the optical filter is much smaller than the bandwidth of the light source; therefore only a small portion of the light power from the source can be used in the demodulation, yielding a poor optical power-efficiency and signal-to-noise ratio (SNR). As a result, the surfaces of the fiber end and the diaphragm inside the cavity had to be coated with metallic thin films to increase the reflected light power. These metallic films make the sensor head susceptible to the strong electromagnetic field inside a high-voltage power.

The research described in this report is determined to overcome these major limitations of our previous work and continue the study toward the development of an integrated fiber optical sensor system for multiplexed PD and hot-spot detections inside high-voltage transformers.

1.3 Technical Approach

The technical approach for multiplexed PD and hot-spots detection is shown in Figure 1-2. The whole system can be divided into two subsystems that are controlled by a computer. The first subsystem is for hot-spot detection achieved by the wavelength division multiplexed fiber Bragg gratings. Many characteristics of Fiber Bragg gratings in temperature measurement such as their large measurement range, high accuracy, and capability of easy multiplexing make them well suited for the particular applications of hot-spot detection inside high-voltage transformers. The second subsystem is for PD detection. Two-wavelength quadrature demodulation method is used to resolve the working point drift problem of the PD sensors. Moreover, under this demodulation method, these PD sensors can be readily multiplexed together as they share the same optical source (two lasers in this case) through the star topology architecture. In this research, we have built and demonstrated a bench-top system at laboratory according the proposed approach. Ultimately, we will translate the bench-top system into a portable and field-test ready instrumentation system as shown in Figure 1-3.

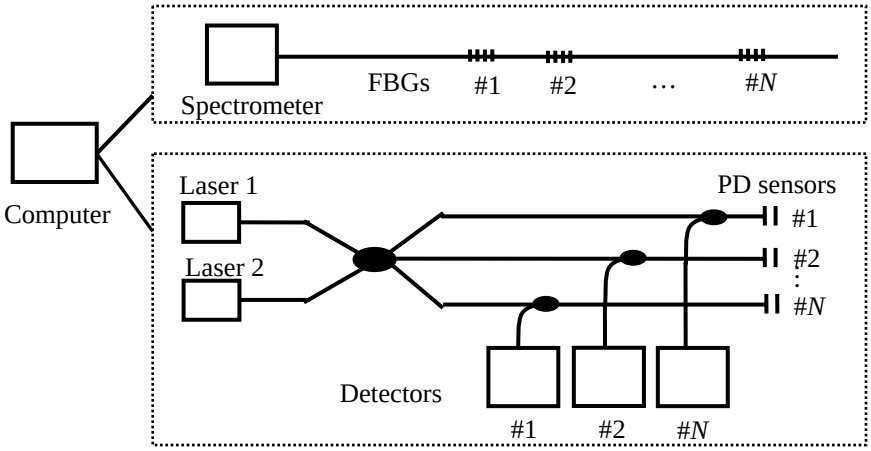

Figure 1-2
Schematic of the Technical Approach Used in the Research

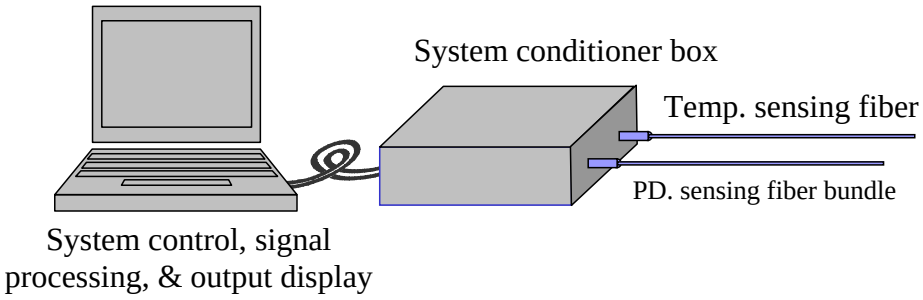

Figure 1-3
Effect View of the Portable and Field-Test-Ready Instrumentation System – which is proposed for development in 2007.

The remainder of the report is organized as follows:

- ***Chapter 2*** is on the subsystem of hot-spot detections. The principle and fabrication are described. Nine sensors are multiplexed together and their performance is tested.

- ***Chapter 3*** deals with the PD sensors. First the principles of both sensor operation and two-laser quadrature demodulation are illustrated. Then we focus on the sensor fabrication based on the laser-fusion bonding. The result of a single sensor test is also provided.

- ***Chapter 4*** is the system implementation. The bench top system built in this project is described and the results of the laboratory demonstration is given.

- Finally, the conclusions and suggestions for future work are given in ***Chapters 5 and 6*** respectively.

2
TEMPERATUE SENSORS

Fiber Bragg grating (FBG) sensors are the most common type of fiber optical sensors that have been intensively studied in the past two decades and widely used for sensing of a wide variety of physical parameters including temperature, strain, and acoustic waves. FBG sensors have all the advantages normally attributed to fiber sensors. In addition, FBGs have an inherent self-calibration capability and can be easily multiplexed in a serial fashion along a single fiber. For temperature measurement, FBG sensors give excellent measurement accuracy and resolution. The operating temperature range of conventional FBGs (<300 °C; otherwise the grating structure will be permanently washed out) perfectly matches the temperature range in high-voltage transformers. Therefore, FBG temperature sensors are well suited for the hot-spots detection in high voltage transformers.

2.1 Principle of Operation

As shown in Figure 2-1 (a), a FBG is created by a periodical variation in the refractive-index of the core of the fiber that has the intended Grating features. As a result, the structure will transmit most wavelengths of light, but will reflect certain specific wavelength. The reflection spectrum of a FBG therefore presents a spike centered at the reflected wavelength as shown in Figure 2-1(b).

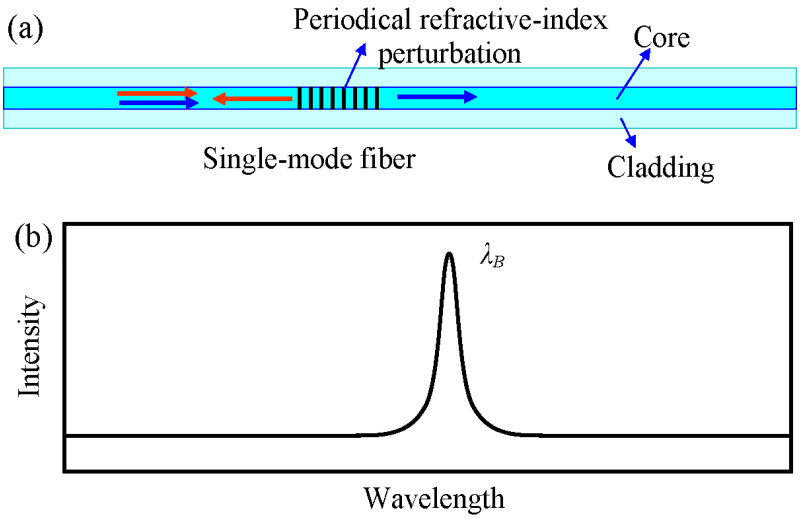

Figure 2-1
Schematic of a Fiber-Bragg-Grating (a); and Its Reflection Spectrum (b)

The reflected wavelength is called the Bragg wavelength, λ_B. The Bragg wavelength is linearly dependent on the period of the refractive index variation or grating pitch (Λ) and the effective refractive index of the fiber (n_{eff}):

$$\lambda_B = 2n_{eff}\Lambda . \qquad (2.1)$$

Both the grating pitch and the effective refractive index of the fiber are temperature dependent. The fiber's effective index can be varied by temperature through the thermo-optic effect; while the perturbation period is varied by temperature through the thermal-expansion effect. A temperature change will cause a shift in the Bragg wavelength; therefore by monitoring the Bragg wavelength, the temperature can be measured. From Equation (2.1), the shift in Bragg wavelength with temperature (T) can be expressed as

$$\Delta\lambda_B = 2n_{eff}\Lambda\left(\alpha + \frac{1}{n_{eff}}\frac{dn_{eff}}{dT}\right)\Delta T , \qquad (2.2)$$

where $\alpha = d\Lambda/dT/\Lambda$ is the coefficient of linear expansion of the fiber; n_{eff} and dn_{eff}/dT can be approximated by the refractive index and the thermo-optic coefficient of fused-silica material, respectively. Using $\alpha = 0.55\times10^{-6}$/°C, $n_{eff} = 1.45$, and $dn_{eff}/dT = 9.1\times10^{-6}$/°C in Equation (2.2), the normalized thermal responsivity is given by

$$\frac{1}{\lambda_B}\frac{d\lambda_B}{dT} = 6.8\times10^{-6}/°\text{C} . \qquad (2.3)$$

In order to resolve a temperature change of ~0.1°C, a wavelength resolution of ~0.001 nm (1 pm) is required at λ_B = 1550 nm.

A wide variety of multiplexing techniques including wavelength division multiplexing (WDM), time-division multiplexing (TDM), and spatial-division multiplexing (STD) have been developed for FBG sensors. Among them, WDM method, in which a number of FBGs with different Bragg wavelengths are written into a single span of fiber as shown in Figure 2-2, is the most straightforward and reliable one. By measuring the reflection spectrum, each of the sensors is simultaneously demodulated in the spectral-domain. In this research, as shown in Figure 2-2, the reflection spectrum from the sensors is measured by a Component Test System (CTS, Micron Optics, Inc.) which performs the measurement with a built-in scanning laser and a detector.

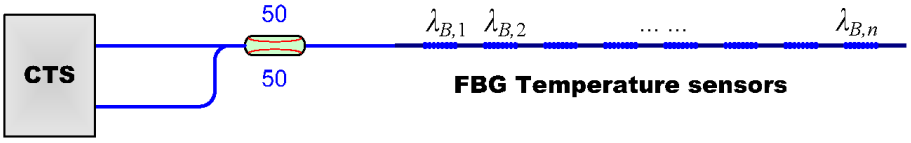

Figure 2-2
Wavelength Division Multiplexing of Fiber Bragg Grating Sensors; CTS, Component Test System

The maximum number of FBG sensors that can be multiplexed in a single fiber by this method is determined by several factors including the temperature measurement range, the available spectral window size, and the shape and bandwidth of the FBG reflection spectrum. The CTS has a spectral measurement range of 50 nm (from 1520 to 1570nm). Assuming that the temperature range to be measured is 200 °C which corresponds to a Bragg wavelength shift of ~2.1 nm according to Equation (2.3), and considering that the bandwidth of a typical FBG ranges from 0.05 to 0.3 nm, a conservative estimate of the spectrum bandwidth each FBG sensor would occupy is 2.4 nm. Therefore, approximately 20 FBG sensors can be multiplexed into the CTS-based sensor system. Note that, due to the narrow linewidth of the built-in scanning laser, the CTS has a high spectral resolution of 0.05 pm, corresponding to a temperature measurement resolution much higher than 0.1 °C, as indicated by Equation(2.3).

2.2 Sensor Fabrication

Traditional FBGs are fabricated with photosensitive fibers whose refractive index experience permanent changes when the fibers are exposed to UV light. We use the hydrogen-loading method to photosensitize the standard telecommunication fibers and use the interferometric method to generate the periodical refractive index perturbations to the fiber.

Hydrogen Loading System

The principle of the hydrogen loading technique is to diffuse the hydrogen (H_2) molecules into the core of a germanium-doped telecommunication fiber at low temperature and high pressure H_2 environment. When the loaded fiber is exposed to UV light, H_2 is thought to be dissociated to form Si-OH and/or Ge-OH bonds, causing the formation of the Ge oxygen-deficient centers and consequently leading to a refractive index change. Compared with commercially available photosensitive fibers, which usually have boron co-doped with germanium in silica glass, there are several advantages of the hydrogen loaded fibers. First, hydrogen loaded fibers demonstrate the largest photosensitive response among all photosensitive fibers. A refractive index change in excess of 0.011 can be easily produced by the UV exposure of standard hydrogen-loaded telecommunication fibers. Second, commercial photosensitive fibers generally are costly ($10-20/meter) and lossy (~30dB/km) compared with standard telecommunication grade fibers (< 6 cents/meter and 0.2 dB/km). In hydrogen loaded fibers, the loaded hydrogen does not stay permanently in the fiber. Once the required increase in photosensitivity is no longer needed, the hydrogen molecules diffuse out so that the ultra-low loss feature of the communication grade fibers is retained.

Figure 2-3
Hydrogen-Loading System

Figure 2-3 shows the hydrogen loading system at CPT, which provides 1100 psi hydrogen pressure at room temperature (23 °C). The length of each session of the fiber that can be hydrogen loaded is limited to 2 m by the length of the steel tubing. However, a large quantity of fiber (i.e. a spool of fiber) can be loaded without discontinuity using a large fiber container. Soaking the fiber for several days in the high pressure hydrogen environment is sufficient to load the 125 micron diameter fiber.

FBG Fabrication System

The multiplexing of FBG sensors requires the fabrication of FBGs with different Bragg wavelengths. We use a phase mask interferometer for the fabrication of FBG sensors. The schematic of the fabrication system is shown in Figure 2-4. The light from a UV laser is normally incident into a phase mask and diffracted into two symmetric directions corresponding to its ±1 order beams. The phase mask is designed in such a way that beams of other orders are suppressed. However, a blocker is used to block the residual 0-order beam. The two refracted UV beams are then reflected by two rotatable mirrors and combine to generate interference pattern, which consequently cause the periodical refraction index perturbations inside the photosensitive fiber. A cylindrical lens is used to focus the light on the fiber.

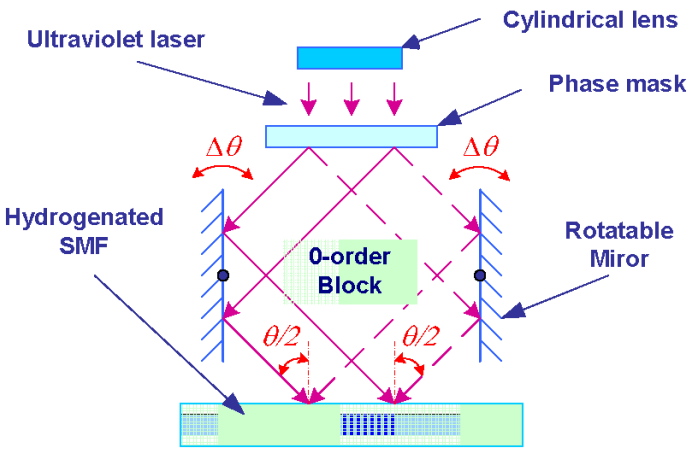

Figure 2-4
Schematic of the Phase Mask Interferometer for FBG Sensor Fabrication

By rotating the mirrors, the period of the interference pattern inside the fiber can be adjusted; therefore FBGs with different Bragg wavelength can be fabricated. The change in Bragg wavelength ($\Delta\lambda$) as a function of the change in the mutual angle between the two interfering mirrors ($\Delta\theta$) is give by

$$\frac{\Delta\lambda}{\lambda_{B0}} = -\frac{\Delta\theta}{2}\cot\frac{\theta}{2}, \qquad (2.4)$$

where θ is the angle between the ±1 order beams; and λ_{B0} is the Bragg wavelength obtained when the two rotatable mirrors are parallel ($\Delta\theta = 0$).

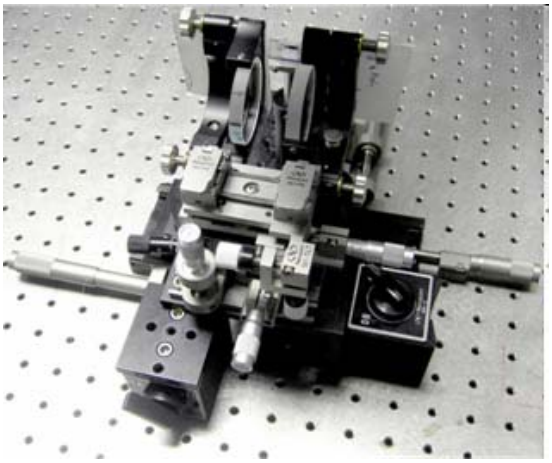

Figure 2-5
A Photograph of the Tunable Phase Mask Interferometer

Using a single phase mask which functions as both a beam splitter and a Bragg wavelength reference, this FBG fabrication method is capable of tuning the Bragg wavelengths in an

extremely large range. For example, with a phase mask at 1550 nm ($\theta \sim 20°$), a change of 5° alters the Bragg wavelength by ~800 nm.

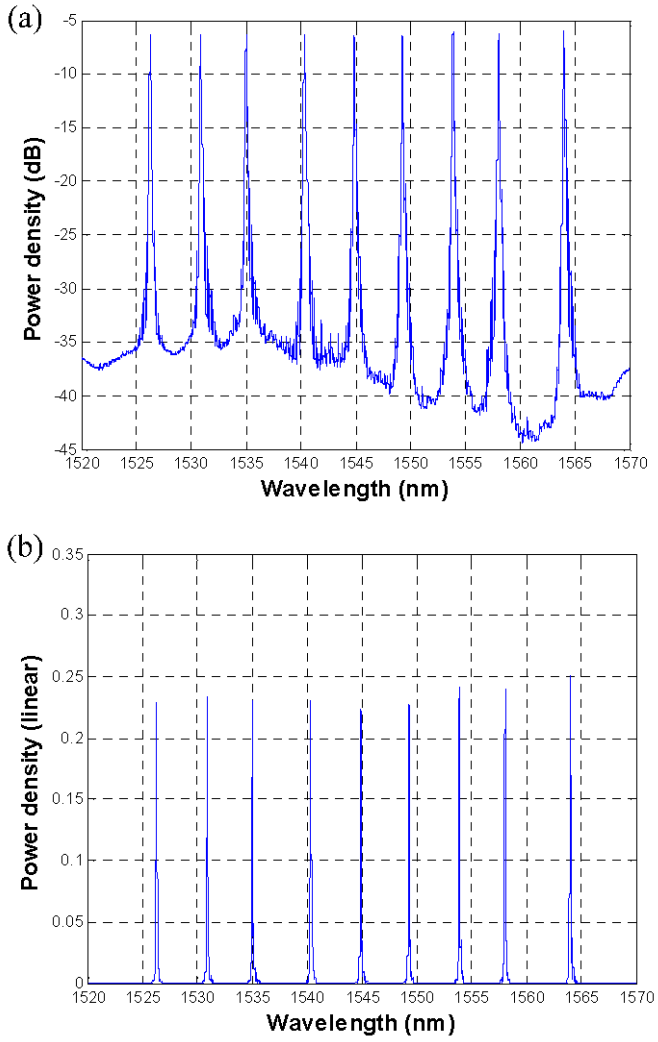

Figure 2-6
Reflection Spectrum of Nine FBG sensors Fabricated In a Single Span of Fiber; (a) In Logarithmic Scale and (b) In Linear Scale

Figure 2-5 shows a photograph of the FBG fabrication set up at CPT. The UV source is a pulsed excimer laser (MPB Communication Inc, MSX-250) operating at wavelength of 248 nm. The repetition rate of the pulse can be varied from 1 to 12 pulses/second and the energy of each pulse is up to 50 mJ. During the fabrication, a CTS and a 2×2 fiber coupler are used to monitor the Bragg wavelength and reflection rate. We have found that mechanical stability of the set up, especially the mechanical stability of the two rotation mirrors, are of great importance to obtain a high reflection rate at the Bragg wavelength. Due to the relatively long interferometric beams, mechanical vibrations can cause significant degradation in the visibility of the interference pattern and therefore greatly reduce the reflection rate of the FBG. By using heavy weight to stabilize the two mirror holders and using long exposure time to the UV pulses, FBGs with near

100% reflection rate can be consistently fabricated. We fabricated nine FBG sensors within the Bragg wavelength range between 1520 and 1570 nm in two spans of hydrogen-loaded fibers with one having 5 and the other having 4 FBG sensors. The two span of fiber was spliced together ad each span is ~1.5 m long. The spectrum of these sensors was captured by the CTS and is shown in Figure 2-6, in both linear and logarithmic scale. Note that a 6-dB power loss is introduced when the light passes through the 2×2 fiber coupler twice; therefore a −6dB power density peak at the Bragg wavelength corresponds to a 100% reflection rate of the FBG. We infer from the reflection spectrum that the reflection rates of the nine FBGs range from 90% to 100%. The spectral bandwidths of the FBGs are uniform, with each having a 3- and 20-dB bandwidth of 0.17 and 0.9 nm, respectively.

Sensor Annealing

The average refractive index of the FBG fabricated on hydrogen-loaded fibers is slightly elevated by the presence of the hydrogen inside the fiber. Over time, as the hydrogen molecules leak out of the fiber, the refractive index continuously decreases, causing the blue shift in the Bragg wavelength. A standard process of annealing, in which the gratings are baked at elevated temperatures for a certain span of time, must be performed before the gratings are tested or used. During the process, the residual hydrogen molecules are driven out of the fiber in an increased speed and the Bragg wavelength can be stabilized for the lifetime of the grating. In addition, the inherently low loss of the standard fiber can be retained as the hydrogen is driven out by the annealing process.

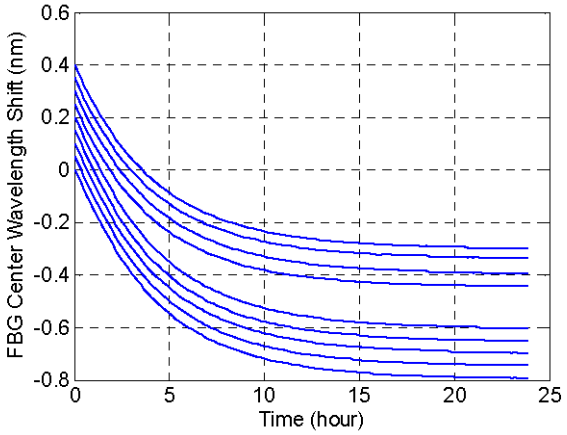

Figure 2-7
Bragg Wavelength Shift during Annealing

The nine FBG sensors were annealed for 24 hours at an annealing temperature of 90 ºC in a temperature chamber. Figure 2-7 shows the shift in Bragg wavelength of each of the nine FBG during the process. After 24 hours, the center wavelengths shift becomes neglectable. It is also seen from Figure 2-7 that Bragg wavelength drift of the nine FBGs falls into two groups. The wavelength drift of FBGs corresponding to the upper four curves is slower than that of the FBGs corresponding to the lower five curves. The reason is that the FBGs corresponding to the lower five curves were written on a piece of hydrogenated fiber that had been kept in the ambient

environment for a much shorter time after it was taken out of the hydrogen loading chamber than the fiber used for the fabrications of FBGs corresponding to the upper four curves. The hydrogen concentrations inside the two fiber were different when they were annealed. The final central wavelength of the FBGs after annealing is sensitive to the hydrogen-loading conditions and history of the fibers.

2.3 Signal Processing

Due to the sensor structure selected, the signal processing procedure is relative simple. Firstly, the reflection spectrum is acquired by a CTS then it is sent to a PC through the GPIB port. Secondly, nine working zones are compartmentalized for each sensing point in the spectrum domain according to the working temperature range. Thirdly, for spectrum of each sensing point, the spectral data is converted to linear scale, and the data points around the center peak (about 15 points) are fitted with a parabolic polynomial, then the center position of the parabola is deemed as the Bragg wavelength of the specific FBG. By comparing this value with the calibration result, the wavelength is converted to the corresponding temperature. This procedure is repeated every one minute to monitor the temperature variance of each sensing point. If any one of the temperatures exceeds the critical temperature threshold, an alert will be given. Because the relation between the temperature change and the center wavelength shift is fairly linear (linearity greater than 99%) within the operational temperature range, the calculation of temperature is given by

$$T = T_0 + S_T^{-1}\left(\lambda - \lambda_0\right), \qquad (1.5)$$

where λ_0 is the Bragg wavelength corresponding to the calibration temperature T_0.

2.4 Temperature Sensor Test

After annealing, the temperature responses of the fabricated temperature sensors, including the temperature sensitivity, stability, and measurement resolution, were tested. Not only did the test results indicate the performance of these particular sensors, but it provide useful information in the design and fabrication of future sensors that are optimized for the field test.

Sensor Responsivity

The responsivity of a FBG temperature sensor is defined as its Bragg wavelength shift cause by a unit temperature change. During the test, the sensors were placed into a temperature chamber which is capable of controlling the temperature with an accuracy of 0.1 °C. The temperature was increased from 25.0 to 80.0 °C at a step of 5 °C. At each step, the reflection spectrum from the sensor series (containing 9 sensors) was recorded by the CTS and the peak position of each sensor was calculated. Figure 2-8(a) shows the Bragg wavelength shift of each sensor (from its Bragg wavelength position at 25 °C) as a function of the temperature. In order to clearly show the result, the lines were shifted in the vertical direction to avoid overlap. The nine lines correspond to the nine FBG sensors (from bottom to top: FBG #1, #2, …, #9). The small fitting

errors of the linear fit and the parallelism between the lines indicates that the temperature responses of all the nine sensors are linear and uniform. The temperature sensitivity of each sensor is estimated by the slope of the corresponding temperature response fitting line and is shown by the heights of the bars in Figure 2-8 (b) for all nine sensors. It is evident that the nine sensors have a similar temperature responsivity of about 0.01 nm/°C.

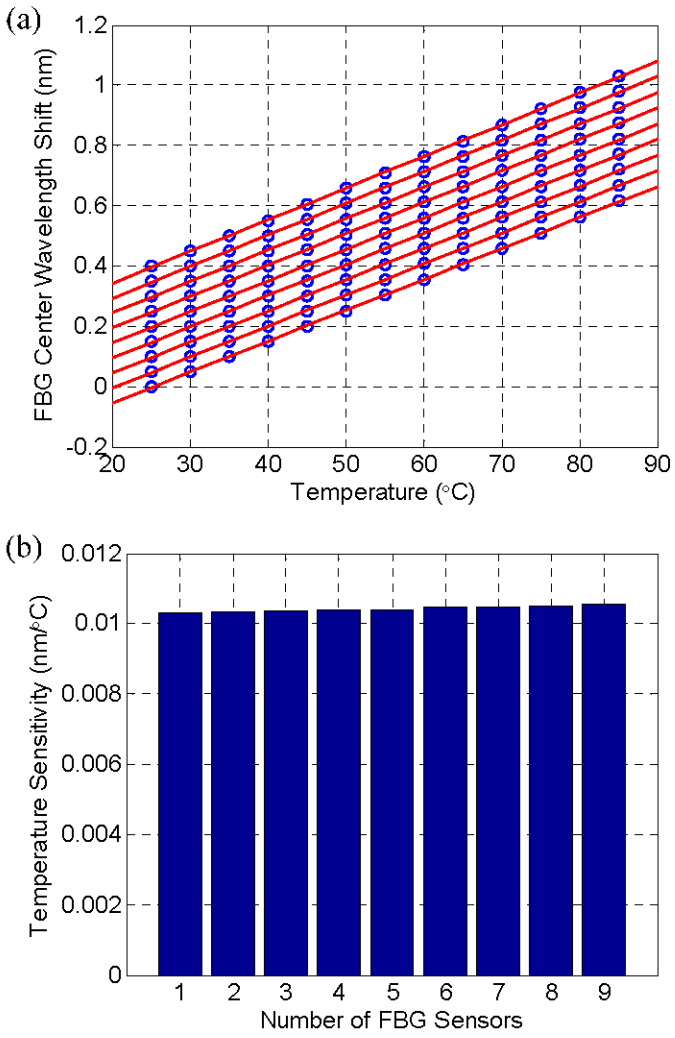

Figure 2-8
Responsivity Test of the Nine Temperature Sensors; (a) Bragg Wavelength Shift versus Temperature Change; (b) Bar Chart of Responsivity Test Results

Sensor Stability

The stability of the FBG temperature sensors can be characterized by the amount of drift in Bragg wavelengths over time at specific temperatures. In this test, the temperature was maintained at a constant level of 40 °C and the spectrum of each of the sensors was continuously recorded for about 24 hours. The Bragg wavelength as a function of the measurement time is shown in Figure 2-9 for each of the sensors (once again, from bottom to top, the FBGs are

numbered as #1, #2, …, #9). There is no observable drift in Bragg wavelength for all the nine FBG sensors during the test time.

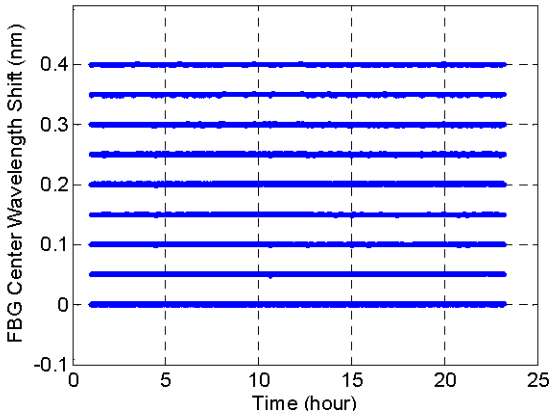

Figure 2-9
Fluctuation of Bragg Wavelengths of FBG Sensors at 40°C over 24 Hours

Measurement Resolution

The measurement resolution of temperature sensors is defined as the minimum difference in temperature that can be separated by the sensor. Using the stability test results described above, the temperature measurement resolution of each sensor is estimated by the standard deviation of the wavelength shift divided by the temperature sensitivity of the sensor which was obtained in Test 1. The result is shown in Figure 2-10. It is clearly shown that each of the sensors has a measurement resolution better than 0.1 °C, which is sufficient for the applications of thermal fault detection in the transformer.

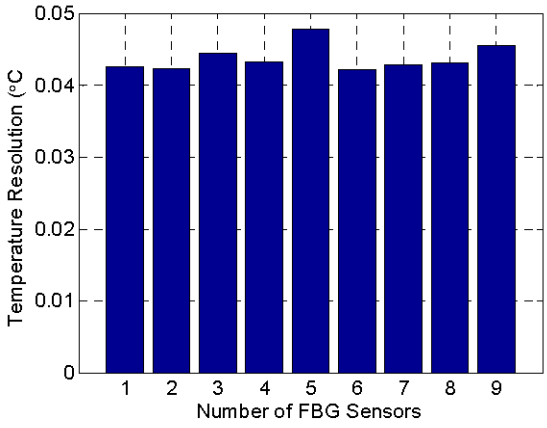

Figure 2-10
Bar Chart of Measurement Resolution of FBG Sensors

3
PARTIAL-DISCHARGE SENSORS

As shown in Chapter 1, the fabrication method of partial discharge (PD) sensor heads previously developed at CPT involves complicated process and the accurate control of cavity length is difficult. Moreover, the signal demodulation is complicated by the use of expensive tunable optical filters. Most importantly, the optical power efficiency is much reduced, which makes difficult the multiplexing of the PD sensors. In this research, new laser bonding method was employed to fabricate the PD sensors. The fabrication is simplified and the repeatability of the fabrication and accuracy of the cavity length control are greatly improved. Two- laser quadrature detection was used for signal demodulation. This demodulation method is more reliable and power efficient. As a result, several PD sensors can be multiplexed. In this chapter, the principle, fabrication and multiplexing of the PD sensors are presented.

3.1 Principle of Operation

We used diaphragm-based extrinsic Fabry-Perot (FP) interferometric sensors for PD detection. The sensor can detect the acoustic waves generated by PD activities inside a transformer. Figure 3-1 shows the schematic of the sensor head, in which the FP cavity is formed by a cleaved end of a single mode fiber and the inner surface of a thin fused-silica diaphragm. The glass tube and the glass ferrule facilitate the alignment of the fiber and the support of the diaphragm. The incipient light from the fiber is partially reflected by the two surfaces of the cavity due to the Fressnel reflection at the glass-air interface. The two reflections then interfere and the interference signal contains the information of the FP cavity length. When PD activities occur, the PD-generated acoustic waves cause the diaphragm, and consequently the FP cavity length, to vibrate. By measuring monitoring the cavity length variations from the interference signal, the acoustic

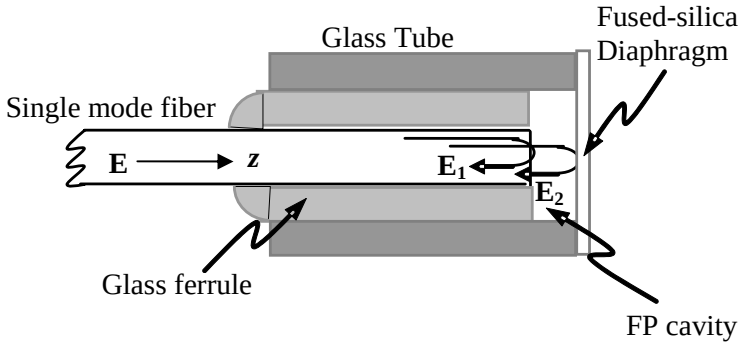

Figure 3-1
Schematic of the Diaphragm-Based PD Sensor Head

waves, and consequently the PD, can be detected.

Assume electrical field of the incipient light is **E**, and the electrical field of the reflections from the fiber end and inner surface of the diaphragm are $\mathbf{E}_1$ and $\mathbf{E}_2$ respectively. Electrical field $\mathbf{E}_1$ can be expressed as

$$\mathbf{E_1} = E_1\hat{\mathbf{z}} = A_1 e^{j(\omega t-\beta z+\phi)}\hat{\mathbf{z}}, \qquad (3.1)$$

where β is the propagation constant of the light in the fiber, A_1, ω, and ϕ are the amplitude, the angle frequency, and the initial phase of the light, respectively. Electric field $\mathbf{E}_2$ travels back and forth inside the FP cavity; therefore comparing to $\mathbf{E}_1$, it has a relative phase shift of $4\pi d/\lambda_0$, where λ_0 is the wavelength of the light in air and d is the FP cavity length. Therefore, $\mathbf{E}_2$ can be written as

$$\mathbf{E}_2 = E_2\hat{\mathbf{z}} = A_2 e^{j(\omega t-\beta z+\phi-4\pi d/\lambda_0+\pi)}\hat{\mathbf{z}}. \qquad (3.2)$$

where A_2 is the amplitude of the light and the extra phase shift of π arises from the reflection at the diaphragm surface of light incident from a medium that is optically less dense to a medium that is optically denser. Since the reflections at both FP surfaces are small (~4% governed by the Fressnel law), the multi-reflections inside the FP cavity can be ignored. The interference signal is detected by a photodetector and the output of the detector is then given by

$$\begin{aligned} I &\approx \left|\mathbf{E_1}+\mathbf{E_2}\right|^2 = \left(E_1+E_2\right)\left(E_1+E_2\right)^* \\ &= A_1^2 + A_2^2 - 2A_1A_2\cos(4\pi d/\lambda_0) \end{aligned}. \qquad (3.3)$$

After filtering out the direct current (DC) signal, the useful alternative current (AC) is given by

$$U = \gamma\cos(4\pi d/\lambda_0), \qquad (3.4)$$

which is a function of both cavity length d and light wavelength λ_0. In Equation (3.4), γ is a constant. The PD-generated acoustic wave causes vibrations in the cavity length of the PD sensor. By measuring the interference intensity, the cavity length can be calculated from Equation (3.4). The sensitivity of the sensor, which defined as the intensity change caused by unit cavity length change, is given by

$$S(d) = \frac{\partial U}{\partial d} = \gamma'\sin\left(4\pi d/\lambda_0\right), \qquad (3.5)$$

where $\gamma' = 4\pi\gamma d/\lambda_0$. Equation (3.5) shows that the sensor sensitivity to the gap-length is sinusoidal function of the gap length and reaches its maximum when

$$d = d_{Qm} = \left(m+\frac{1}{2}\right)\frac{\lambda_0}{4} \quad m = 0,1,2.... \qquad (3.6)$$

Note that the cavity length change Δd caused by the PD-generated acoustic waves are much smaller than the light wavelength λ_0, or $\Delta d << \lambda_0$. The response of the detector is approximately linear in the vicinity of each d_{Qm}. These d_{Qm} are called the operating points or *Q* points of the sensor.

Due to the thermal expansion and the static background pressure of the transformer oil, the original cavity length d or the working point can slowly drift from the optimized point, causing degradation in the sensor sensitivity. Therefore, the working point must be carefully controlled during the sensor operation. Previously a tunable laser or filter is used to adjust the wavelength of the probing light according to the sensor cavity length. However, the required tunable lasers or tunable optical filters are costly and the multiplexing of sensors is difficult. In order to avoid these problems, two-wavelength quadrature detection is used in this research – and this step forward represents one of the significant research advances in this work in 2006.

3.2 Two-wavelength Quadrature Demodulation

Two-wavelength quadrature demodulation uses two lasers with different wavelengths as the light sources. Assume an arbitrary wavelength $\lambda=\lambda_0+\Delta\lambda$, where $\Delta\lambda$ is the deviation from a reference wavelength λ_0 and satisfies $\Delta\lambda << \lambda_0$; then from Eq. (3.4), the normalized response of the sensor is approximately a cosine function of $\Delta\lambda$ which is given by

$$U\left(\lambda_0+\Delta\lambda, d\right) \propto \cos\left[4\pi d\left(\frac{1}{\lambda_0}-\frac{\Delta\lambda}{\lambda_0^2}\right)\right] = \cos\left(\theta - 4\pi d\cdot\Delta\lambda/\lambda_0^2\right) \qquad (3.7)$$

where $\theta=4\pi d/\lambda_0$. The period of the sinusoidal wave is

$$\lambda_d = \frac{\lambda_0^2}{2d} \qquad (3.8)$$

Figure 3-2(a) and (b) shows the normalized sensor response as a function of the laser wavelength change $\Delta\lambda$ at two different cavity length d and d'. When $|d-d'| << d$, the periods of the sinusoidal curves shown in Figure 3-2(a) and (b) are approximately equal. In two-wavelength quadrature demodulation, the wavelengths of the lasers, λ_1 and λ_2 are selected in such a way that

$$\lambda_2-\lambda_1 = \frac{\lambda_0^2}{4\pi d}\frac{\pi}{2} = \frac{\lambda_0^2}{8d}, \qquad (3.9)$$

which is a quarter period of the sinusoidal curve. Figure 3-2 gives one example of such a pair of quadrature wavelengths. In such a case, wavelength λ_1 yields the maximum sensor sensitivity while wavelength λ_2 gives the minimum sensitivity (=0). When the cavity length shifts, the sensor sensitivities corresponding to both wavelengths are varied. However, at least one wavelength gives a sensitivity better than 0.707 of the maximum sensitivity provided $|d-d'| << d$

is satisfied. In the operation of the sensor, signals corresponding to different lasers can be separated by a fixed optical filter. The worst sensitivity of the whole system occurs at the cavity lengths where the two wavelengths give equal sensitivity of 0.707 as shown in Figure 3-2(b).

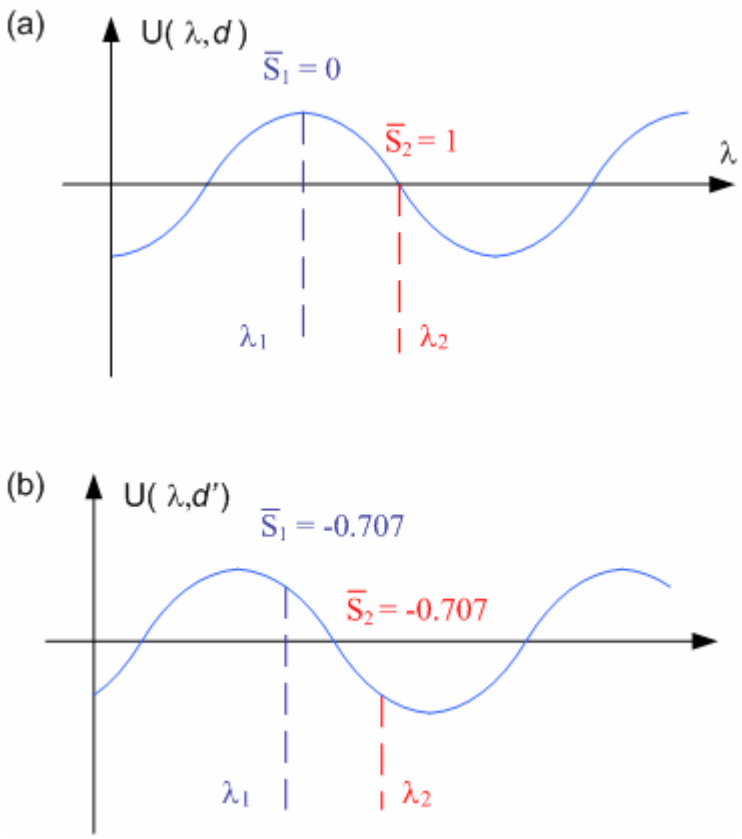

Figure 3-2
Two-laser quadrature detection (*d*~*d'*) (a) the best condition; (b) the worst condition

Compared with the traditional *Q*-point control methods which involve tunable lasers or tunable optical filters, two-wavelength demodulation significantly reduced the total system cost. In addition, the stability and robustness is greatly increased without moving parts involved. Moreover, the optical power of the lasers is more efficiently used than tunable filter-based *Q*-point control in which only a small part of the light is used as the probe light.

Note that we have assumed that $|d - d'| << d$ in the above discussions. In such a case, the two wavelengths remains to be quadrature during the cavity length shift. However, when the environment induced sensor cavity length change is too large so that the approximation of $|d - d'| << d$ is not valid any more, the original two wavelength may depart from being quadrature. In such case, the worst sensitivity of the whole system may be reduced. In the following discussion, we calculate the cavity length range that the system can maintain a specific sensitivity.

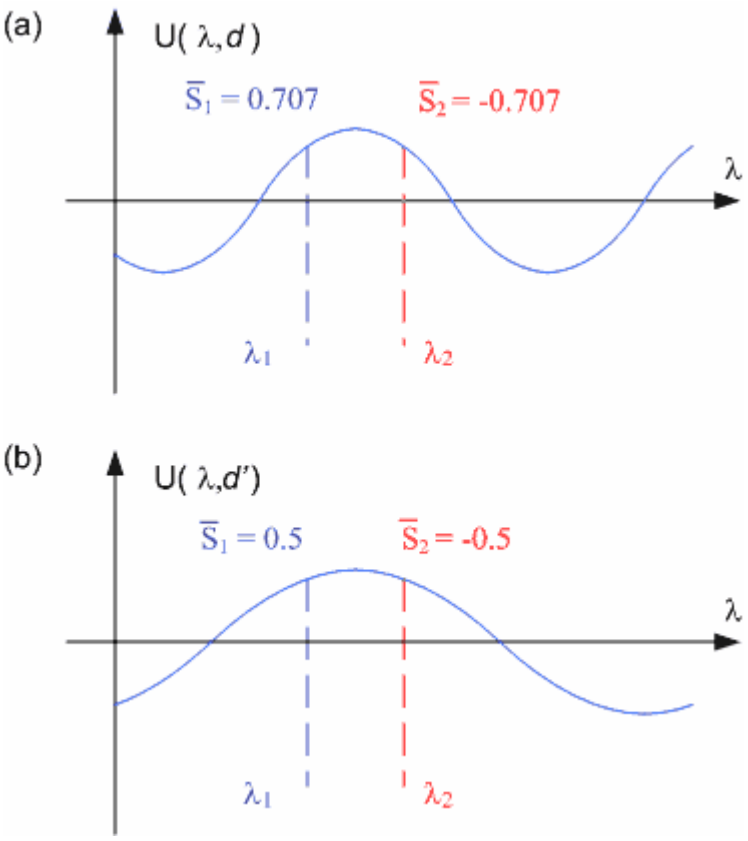

Figure 3-3
Tow-laser quadrature detection (*d*>*d'*) (a) the worst condition without background pressure; (b) the worst condition with background pressure.

We assume the worst normalized sensitivity is decreased from 0.707 to 0.5 due to the increase of the period of the spectral response of the FP sensor, as shown in Figure 3-3. In the condition shown in Figure 3-3 (a) we have

$$\Delta\lambda = \lambda_2 - \lambda_1 = \frac{\lambda_d}{4} = \frac{\lambda^2}{8d}, \qquad (3.10)$$

and in the condition shown in Figure 3-3 (b) (assume minimum acceptable normalized sensitivity of 0.5) we have

$$\Delta\lambda = \lambda_2 - \lambda_1 = \frac{\lambda_d'}{6} = \frac{\lambda^2}{12d'} \qquad (3.11)$$

where λ_d' and d' are the changed fringe period and sensor cavity length respectively. Eqs.(3.10) and (3.11) lead to

$$\frac{d'}{d} = \frac{\lambda_d}{\lambda_d'} = \frac{2}{3}, \qquad (3.12)$$

which indicates that the static-pressure-induced cavity length change must be smaller than 1/3 of the original cavity-length to guarantee the sensitivity is better than 0.5. Therefore, for a highly sensitive diaphragm-based PD sensor, which gives larger cavity length change for certain sound pressure, a longer cavity length should be used. However longer cavity length makes difficulty to the separation filter design because the two wavelengths are closer as shown by Equations. (3.10) and (3.11), requiring a faster roll-off separation filter to separate the signal corresponding to the two lasers. Typically the CWDM add/drop multiplexer has 20dB attenuation at 7nm away from the center wavelength (the central wavelength is 1550nm for our system). Therefore, from Equation (3.10) the maximum cavity length due to this requirement is

$$d_{\max} = \frac{\lambda^2}{8 \cdot \Delta\lambda} = \frac{1550^2}{8 \times 7} = 43\mu\text{m} \qquad (3.13)$$

In order to monitor the cavity length during fabrication, we need at least one fringe (one period: λ_d) inside the spectral measurement window of the CTS, which is a 50 nm span centered at λ_0 = 1545 nm. From Equation (3.8) the minimum cavity length is given by

$$d_{\min} = \frac{\lambda_0^{\,2}}{2\lambda_d} = \frac{1545^2}{2 \times 50} = 24\mu\text{m} \qquad (3.14)$$

Considering these requirement, we select the cavity length d = 40μm. From Equation(3.8) the corresponding period of the spectral response λ_d = 30 nm. By using Eq. (3.12), the permitted maximum cavity length change is

$$\Delta d = d' - d = -\frac{d}{3} = -\frac{30}{3} = -10\mu\text{m}\,. \qquad (3.15)$$

For the designed PD sensor that has a diaphragm diameter of 1.8mm and thickness of 75μm, the theoretical diaphragm sensitivity is 4 nm/kPa; therefore, if the background pressure is 1bar, the corresponding cavity length change is only –0.4 μm, which is much less than the value given by Eq. (3.15). In this condition, the normalized minimum sensitivity is very close to 0.7.

3.3 Sensor Structure and Fabrication

A PD sensor with new dimensional parameters has been designed. Figure 3-4 (a) shows the structure of the sensor head and Table 3-1 gives the dimensions of the ferrule, sleeve. The thickness of the diaphragm is 75μm.

Table 3-1
Dimensions of Key Components of The Sensor Head

	I.D (μm)	O.D (mm)	Length (mm)
Ferrule	127	1.8	6
Sleeve	1815	2.8	3

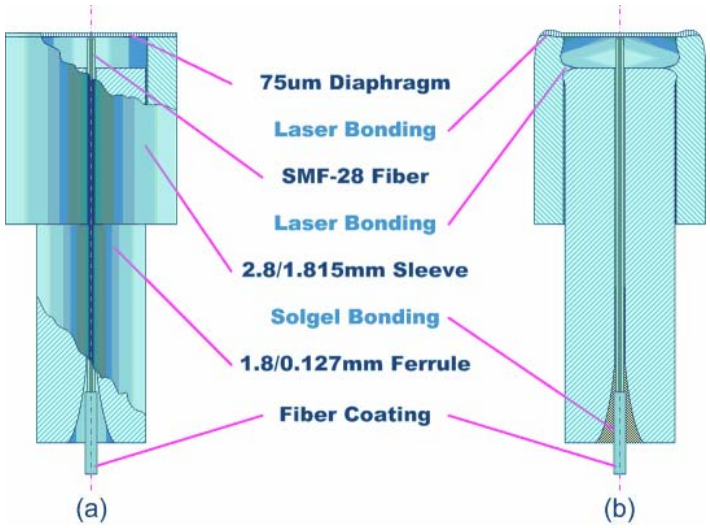

Figure 3-4
Sensor Head Structure and Bonding (a) Schematic of Sensor Head; (b) Cross-Section View of the Sensor Head After Laser And Sol-Gel Bonging

Based on the diaphragm theory[4] the sensitivity of sensors depicted in Figure 3-4 is given by

$$\delta = 2.524\times10^{-6}\frac{a^4}{h^3}(\text{nm/kPa}), \qquad (3.16)$$

where a and h are the radius and thickness of the diaphragm in μm respectively. The resonant frequency of the diaphragm is given by

$$f_0 = 2.72\times10^{6}\frac{h}{a^2}(\text{kHz}). \qquad (3.17)$$

Using the parameters listed in

[4] *Development of a Prototype Fiber-Optic Acoustic PD Sensor: For Inside Transformer Installation*, EPRI, Palo Alto, CA: 2001. 1001943

Table 3-1 in Equations (3.16) and (3.17), the sensitivity and the frequency response as functions of the diaphragm thickness are plotted in Figure 3-5. It is evident that there is a trade-off between the sensitivity and resonant frequency in choosing the diaphragm thickness. In this project, h = 75 μm is selected, corresponding to a sensitivity of 3.9 nm/kPa and a resonant frequency of 252 kHz. (The frequency of the PD-generated acoustic waves usually is in the range of 20~200 kHz.)

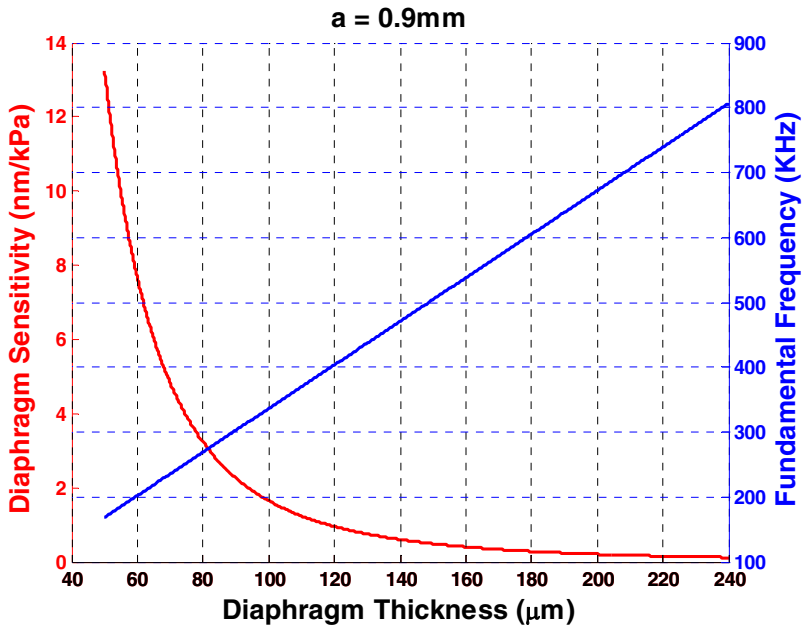

Figure 3-5
Sensitivity and Resonant Frequency vs. Diaphragm Thickness

Note that Eq.(3.16) is only valid when the deflection is not less than 30% of the thickness of the diaphragm, the maximum operating pressure is given by

$$P_{\max} = 0.3h\delta = 0.3\times 75\times 10^{3}\times 3.9 = 8.8\times 10^{4}(\text{kPa}), \tag{3.18}$$

which is much greater than the maximum pressure inside a transformer under normal conditions.

CO_2 laser thermal weld is used to bond the diaphragm, the sleeve and the ferrule together to make a sensor head. A cleaved fiber is bonded to the sensor had with sol-gel process. The setup for the fabrication of the PD FP sensor is shown in Figure 3-6 (a). Firstly a ferrule and a sleeve are welded together, and then the step motor driven rotor is adjusted to the vertical position to perform the diaphragm weld. At last, a bare fiber with cleaved end is inserted into the bonded sensor head and after the cavity length between the fiber tip and the inner surface of the diaphragm is adjusted to the desirable value using a translation stage, sol-gel is placed at the flare of the ferrule, and then a low power laser is applied to solidify the sol-gel. Because the bonding temperature is low, the fiber and its coating are still intact after bonding. Figure 3-6 (b) shows the close up picture of a finished PD FP sensor.

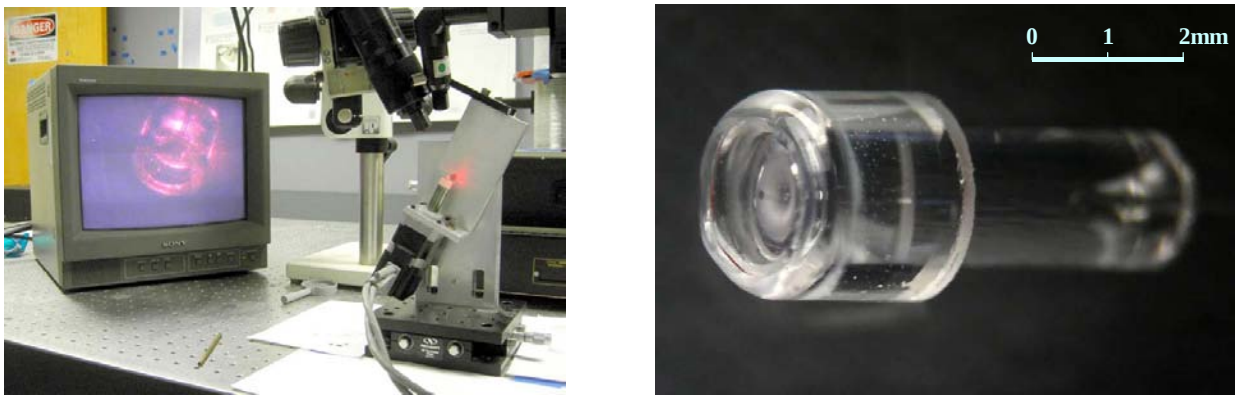

(a) (b)

Figure 3-6
PD FP sensor fabrication (a) sensor fabrication setup; (b) close up picture of a PD FP sensor.

The reflection spectrum of a PD FP sensor is given in Figure 3-7, from which the visibility of this sensor is calculated to be about 96%.

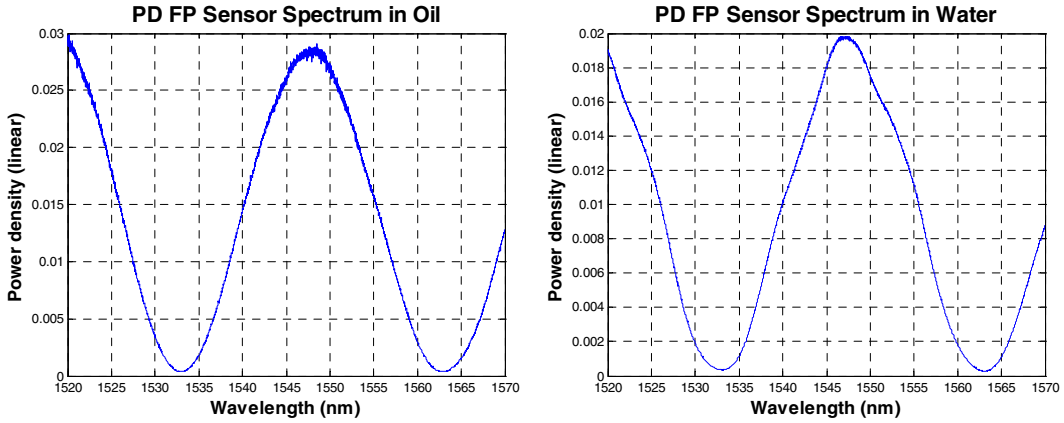

(a) (b)

Figure 3-7
Reflection spectrum of a PD FP sensor in (a) transformer oil; (b) water

3.4 Optical Receiver Circuits

The optical receiver includes the photodectector and its following amplification circuits. The circuits need special design according to many parameters including the intended signal intensity and spectral bandwidth. In this project, we designed and built the optical receiver circuit, shown in Figure 3-8. The circuit includes one stage of transimpedance amplifier and two stages of identical bandpass filters. Because two lasers at different wavelength are used to probe each PD

sensor, two identical receiver circuits are used to detect and amplify the light signal from each PD sensor.

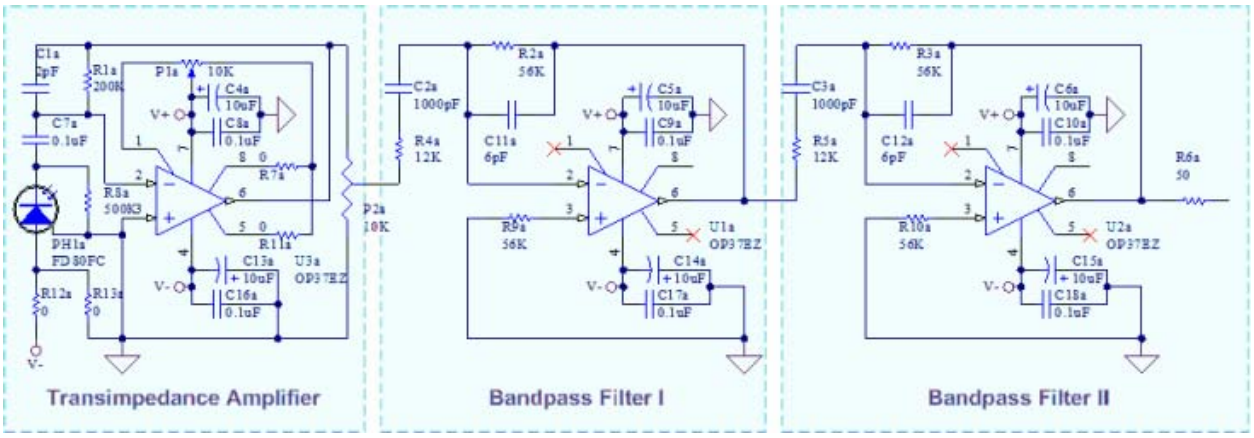

Figure 3-8
Optical Receiver Circuit.

The gain of the transimpedance amplifier is $G_{I\text{-}V} = 2\times10^5$ V/A, and the gain of the bandpass filter is $G_B = 10$. According to the requirement on the PD detection, the pass band of the entire receiver is designed to be from 20 to 300kHz to cover the whole bandwidth of the PD-generated acoustic waves. The measured frequency response of the receiver is shown in Figure 3-9 (a).

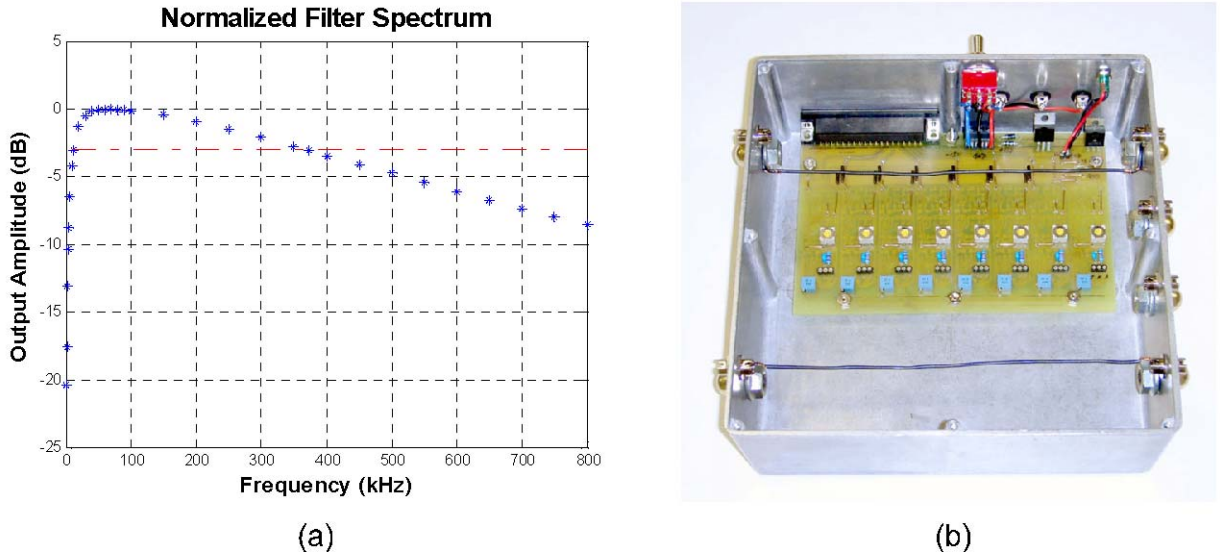

Figure 3-9
(a) Optical Receiver Frequency Response; (b) Assembled 8-route Optical Receivers

Because 4 PD sensors were used in the PD detection system, 8 identical receiver circuits were required and built. All of the circuits were sealed in a casting Aluminum box to isolate possible EMI. Figure 3-9 (b) shows the picture of the assembled 8-route optical receivers.

3.5 Single Channel PD Detection

In order to check the efficiency of the quadrature detection, A PD detection module with single channel (single PD sensor) was built and also a static pressure test bench was built to provide similar pressure environment inside a transformer. The schematic of the PD detection module is shown in Figure 3-10 and a picture of the setup is given by Figure 3-11.

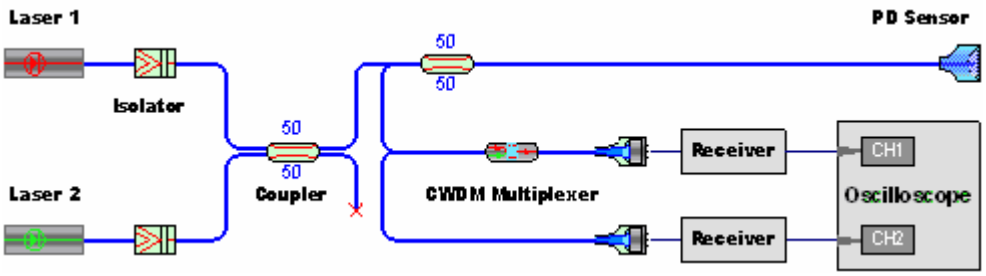

Figure 3-10
Schematic of Single Channel PD Detection

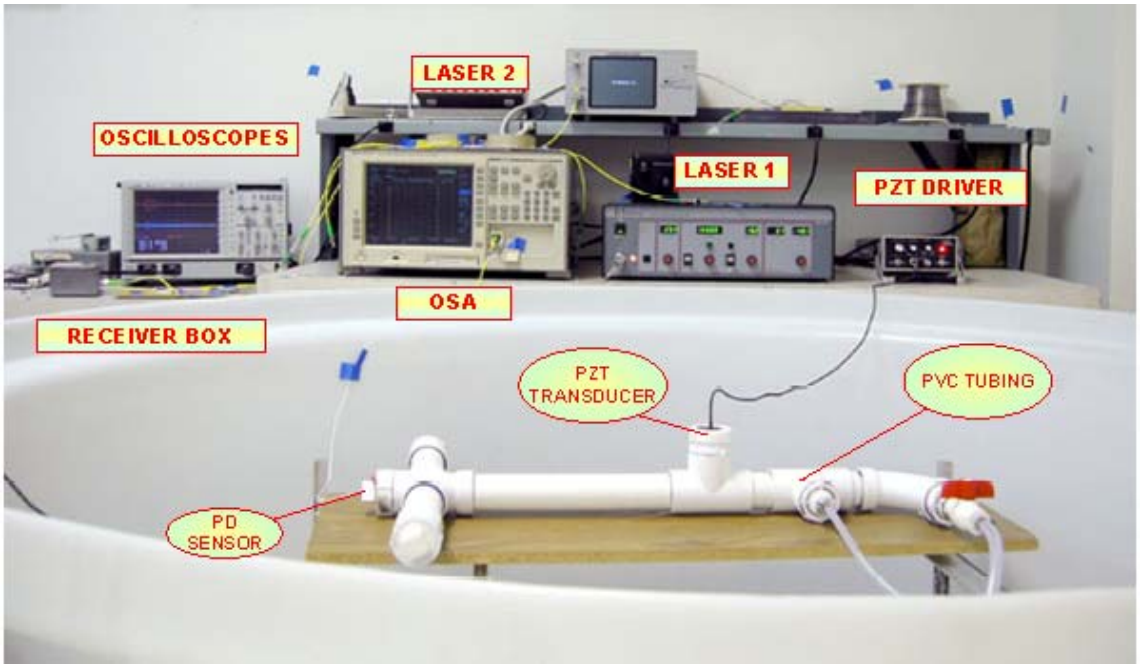

Figure 3-11
Picture of the Single Channel PD Sensor Test System

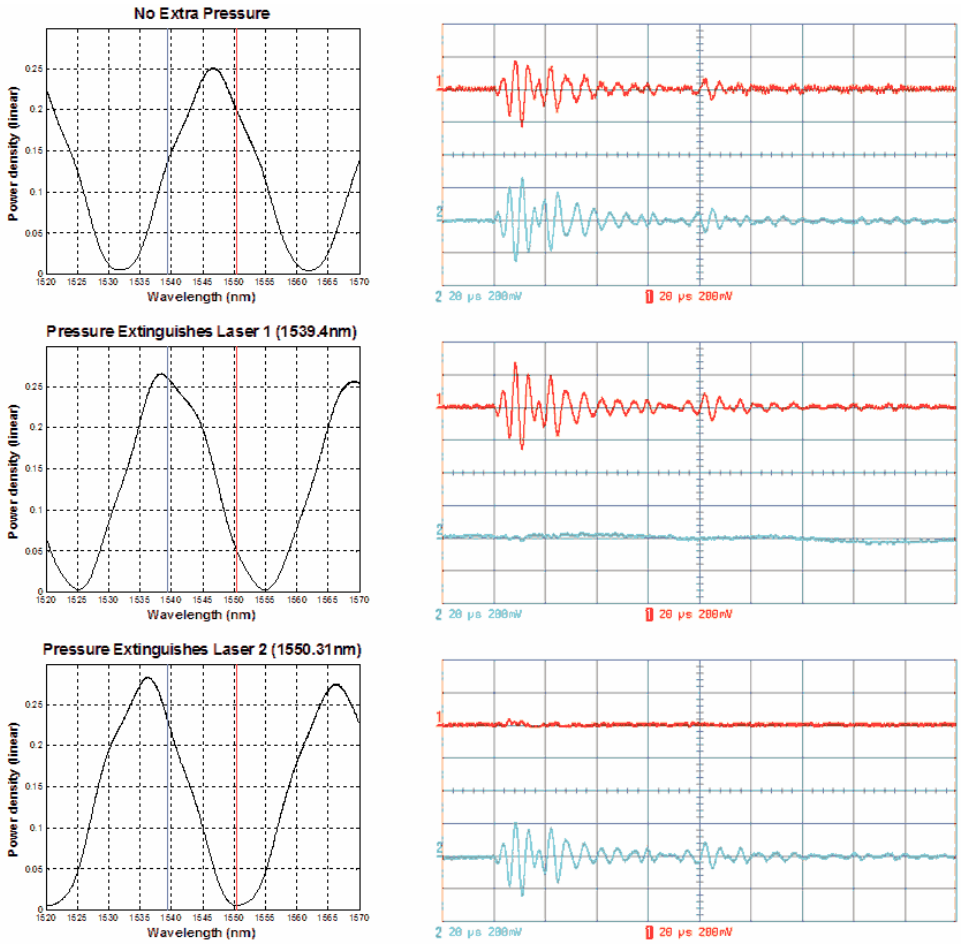

Figure 3-12
Spectra and Output Signal from a PD Sensor in Three Conditions

In the experiment, a PD sensor and an ultrasonic transducer were sealed inside the PVC tube shown in Figure 3-11. The tube was filled with water and the pressure of the water inside can be adjusted by controlling the valve of a faucet connected to the tube by a hose. Two tunable lasers (Laser 1 and Laser 2) were used as shown in Figure 3-10 and their wavelengths were set to be 1539.4 and 1550.3 nm respectively. The output powers of the two lasers measured by an Optical Spectrum Analyzer (OSA) were adjusted to be the same. The PD signals were acquired by the oscilloscope at three different pressures: (1) without extra pressure; (2) the pressure which extinguishes the reflection signal of Laser 1; (3) the pressure which extinguishes the reflection signal of Laser 2. At each pressure, signals from both channels and the reflection spectrum of the PD sensor were recorded. Figure 3-12 shows the results corresponding to pressure conditions (1) to (3). It is clear that independent of the background pressure, a strong PD signal was detected either from channel 1 or channel 2, which verifies the efficiency of the two-laser quadrature detection.

4
SYSTEM IMPLEMENTATION

After the temperature sensors and partial-discharge (PD) sensors had been fabricated and tested, a complete bench top system for on-line multipoint monitoring of both hot-spots and PD activities was built and demonstrated. In this chapter, the schematic, realization, primary test results are presented. In addition, a comparison between the optical PD sensor and an electric PD sensor is given.

4.1 Schematic of the Entire System

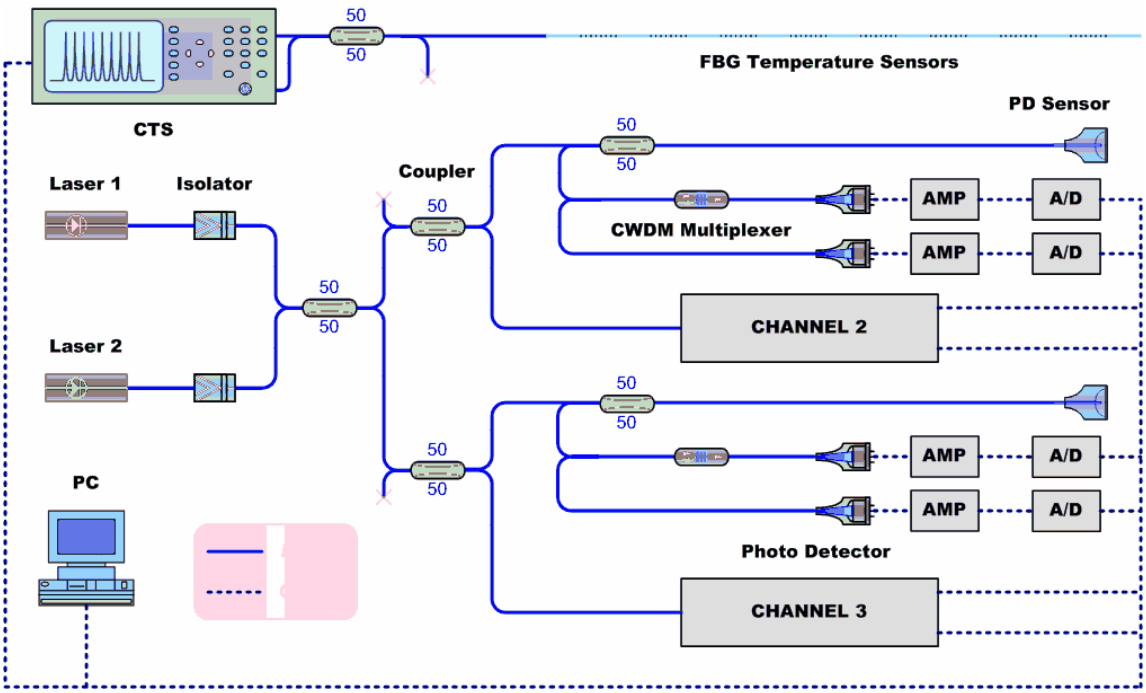

Figure 4-1
Schematic of the Bench-Top System

The schematic of the completed bench-top system is shown in Figure 4-1. The reflection spectrum of the FBG sensors, which was used to obtain the multi-point temperature information, is acquired by a CTS and then sent to a computer through the GPIB port for signal processing. The PD detection subsystem includes four PD sensors. Lights from the Laser 1 and Laser 2 are distributed into the 4 PD sensors through several stages of 3-dB fiber optic couplers. For each channel of the PD detection, the reflected laser light from the PD sensor is separated by a coarse

wavelength division multiplexer (CWDM); and then an optical receiver with a transimpedance amplifier and two bandpass filters is used to convert and amplify the optical signal into AC electric signal. A multi-channel A/D acquisition card is used to convert the analog signal into digital data flow and sent it to the computer. After the digital data of both the temperature detection and PD detection are processed and analyzed by the computer. A user-friendly interface displays the temperature corresponding to each sensing point and the acoustic wave signal of the captured PD discharge, so that the combination detection of temperature and partial-discharge inside a transformer is achieved.

4.2 Bench-top Demonstration System

In order to reduce the ambient interference, the PD detection module including 7 optical couplers, 4 CWDMs, 8 photodetectors, and 8 sets of optical receivers were placed inside a casting aluminum box, as shown in Figure 4-2. The optical inputs of this module are two lasers at 1550 and 1562 nm; the 4 optical outputs are connected to the 4 PD FP sensors; the power inputs are ±15V and ground; the 8 outputs of the optical receivers and a ground are integrated inside a male DB37 connecter, which is the interface to the A/D card.

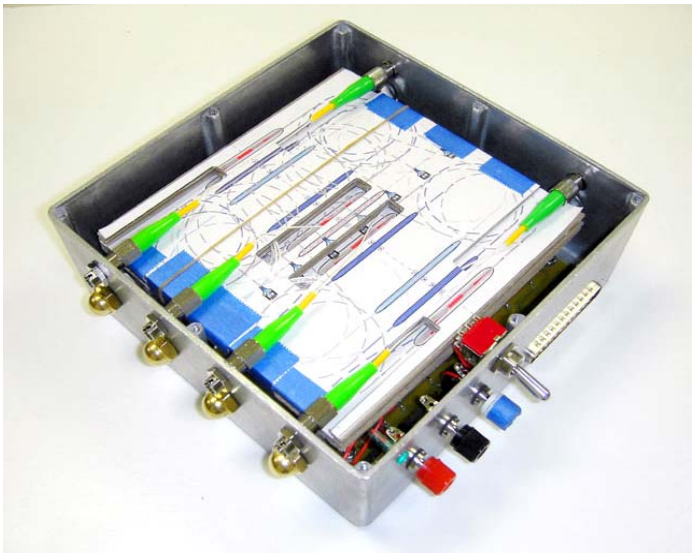

Figure 4-2
PD Detection Module

Finally, we built and demonstrated a complete optical system with both PD and temperature detection for transformer on-line monitoring as schematically shown in Figure 4-1 . Four points of PD detection and nine points of temperature detection were integrated in this system and a plastic tank filled with water was used to simulate the environment inside a transformer. A picture of the real system is shown in

Figure 4-3.

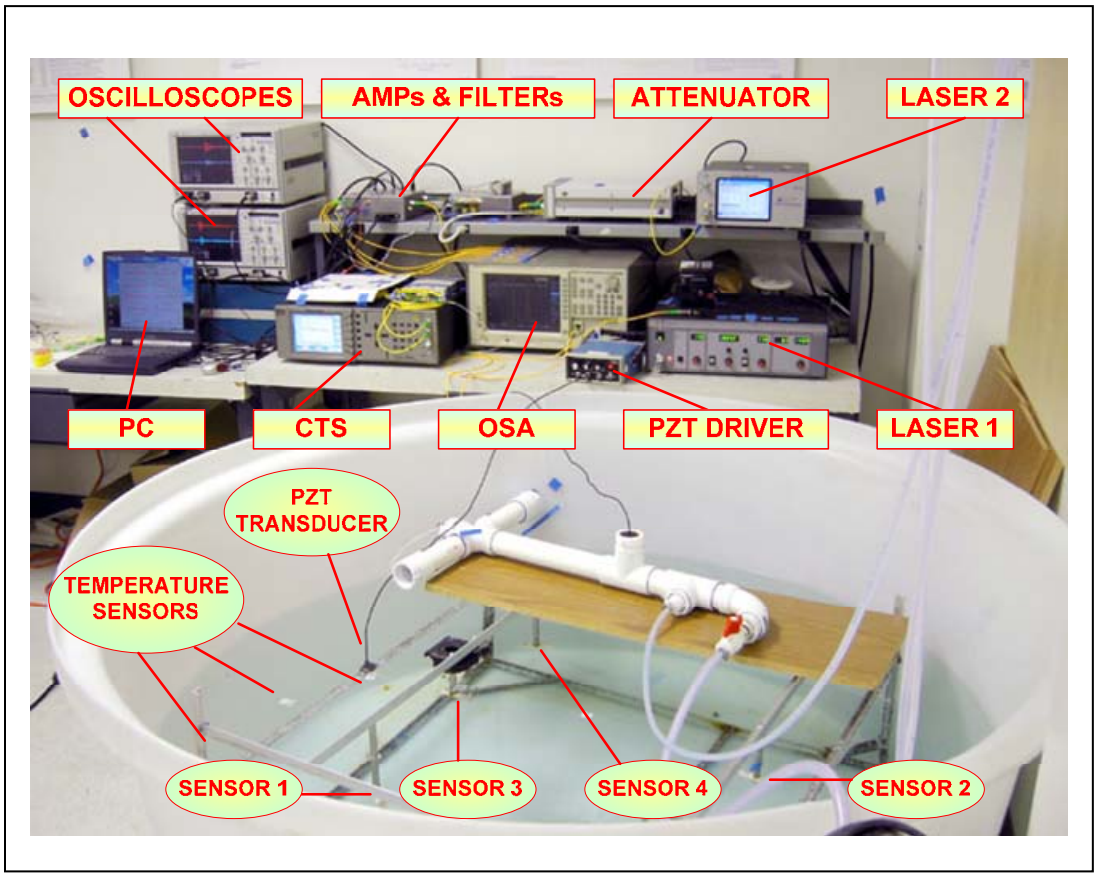

Figure 4-3
Picture of Bench-top System

4.3 Comparison with Electronic Acoustic Sensors

Comparing to PZT acoustic sensors which can only be placed out of transformers, the most prominent advantage of optical PD sensors is their ability to be placed inside the transformers resulting from their inherent immunity to the strong EMI. The PD-generated acoustic waves are much stronger inside the transformer than outside as most of the acoustic energy can be reflected back into the transformer by the transformer wall. Moreover, the optical sensors internal to the transformer will also be much closer to the PD source, and hence see a stronger signal. Given the inherent high sensitivity to acoustic waves of our PD sensor, we anticipate that our PD sensors can pick up weak PD signals that are difficult to be detected by conventional electronic acoustic detectors. In order to give a clear picture of this advantage, we have done the following three tests with both our optical sensors and a conventional PZT sensor. The PZT sensor was purchased from Physical Acoustics Corporation (PAC) (Model: WDU).

Test 1: Optical Sensor Inside Tank and PZT Sensor Outside Tank

The first test is designed to simulate the sensor applications in real transformers. The test setup is schematically shown in Figure 4-4. We used a tank filled with water to simulate a transformer filled with transformer oil. As optical sensors are immune to EMI, they can be placed inside the transformer. Therefore we immersed the optical sensor into the water inside the tank. The PZT sensor was placed on the outside wall of the tank, using grease gel between the sensor and the wall for better acoustic wave coupling, the same way as used in real transformers for such sensors. The PZT transducer, which was used to generate the acoustic waves, was also placed inside the tank, simulating the PD source. The distance between the source and the optical sensor was about 20 cm, while the distance between the source and the PZT sensor was about 100 cm. Signals from both sensors were amplified by a preamplifier (PAC 1220A) and the gain is set to 60dB. An oscilloscope was used to capture the amplified signals as shown in Figure 4-5, the signal from the optical sensor is much stronger than that from the PZT sensor.

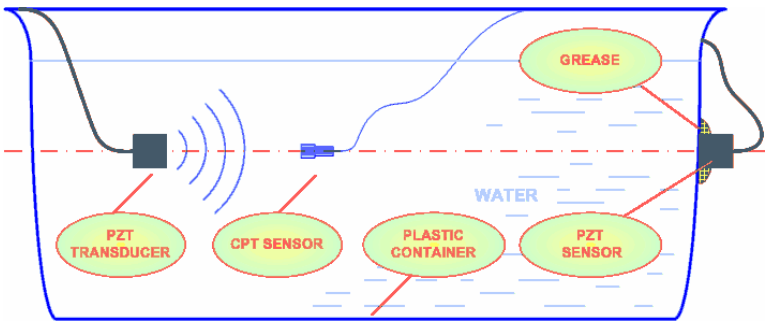

Figure 4-4
Relative Positions of the PD Source, Optical Sensor and PZT Sensor

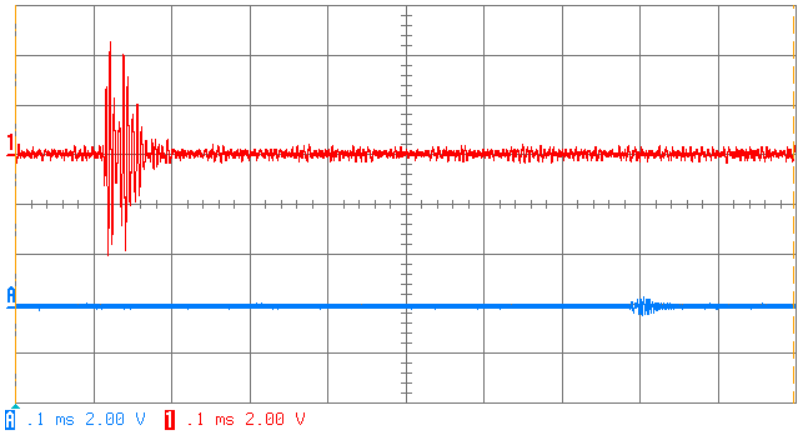

Figure 4-5
Amplified Signals from the Optical Sensor (top trace) and PZT Sensor (bottom trace)

However, the signal-to-noise ratio (SNR) may be more meaningful in comparing sensor performances. In order to calculate the SNRs for both sensors, we measured the output signal of both sensor systems when the PZT transducer was shut down (no signal) and calculated the root-mean-square (rms) value of signal which was used to approximate the noise power. We used the peak-to-peak voltage value to approximate the signal power. The signal and noise signals for both systems are show in Figure 4-6. The calculated SNR of the optical sensor is 17.7dB and that of the PZT sensor is 12.2dB. The SNR of the optical sensor system was 5.5 dB better. However, this was mainly due to the much stronger acoustic waves seen by the optical sensor. Most of the noise of the optical sensor system came from the laser we used and the transimpedance amplification immediately following the photodetector. Theoretically, the optical sensor system can have a much better SNR if a low-noise laser and a low-noise amplifier are used.

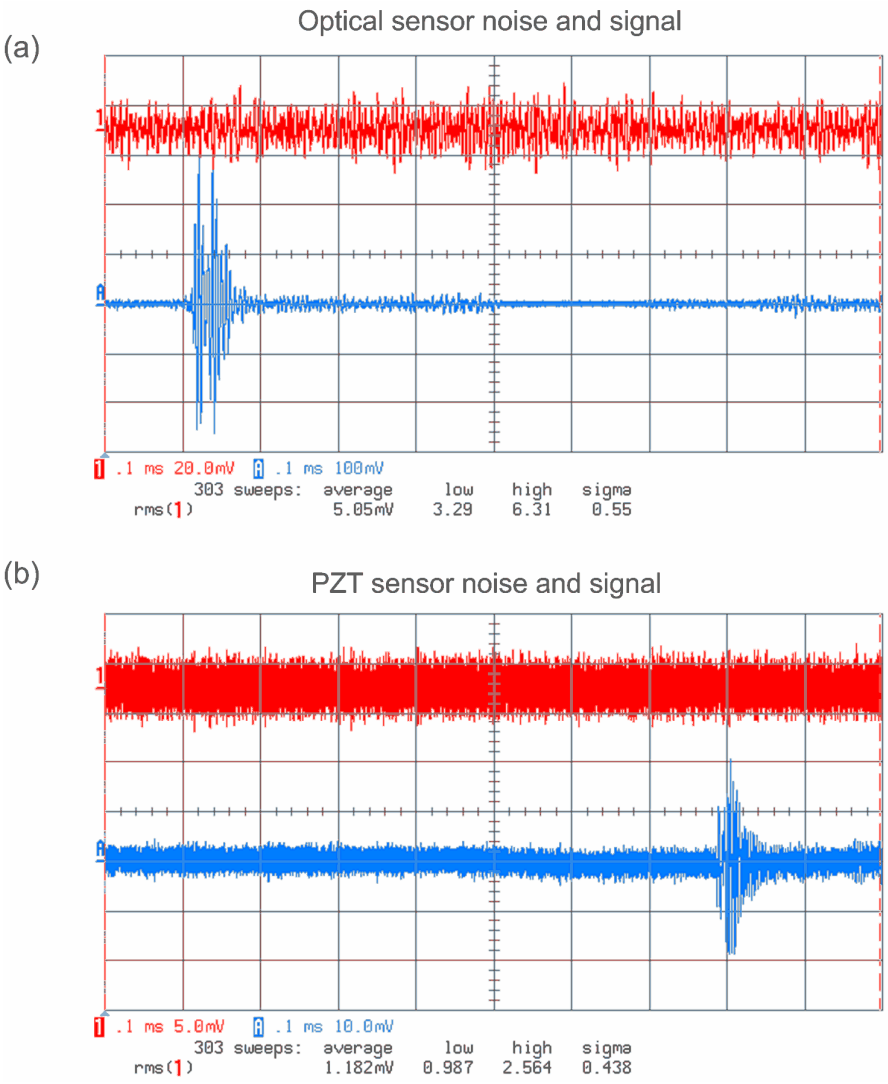

Figure 4-6
A Signals and Noises from (a) Optical Sensor and (b) PZT

Test 2: Reflection Loss due to Tank Wall

It is reported that in real transformers, as much as 90% of the acoustic power can be reflected back into the transformer by the transformer wall (see Footnote 1, Page 1-2). In this test, we measured the reflection loss due to the wall of the plastic tank used to simulate the transformer. Since the tank used is made from a plastic material, its acoustic properties might be quite different from the real transformer material which is usually steel. Moreover, the thickness of the tank wall was only 10 mm; while transformer walls could be much thicker. In this test, we first measured the acoustic wave using the PZT sensor which was attached against the outside wall of the tank with grease gel in between for acoustic coupling. Then we moved the same PZT sensor inside the tank and immersed it in the water. The sensor was placed near to the position where it was placed outside the tank; therefore, the distance effect can be ignored in the acoustic power difference between these two positions The output signals from the same sensor at the two

different positions is shown in Figure 4-7. Surprisingly it indicates that the wall of the plastic container conducts the ultrasonic wave so well that there is almost no attenuation to the acoustic wave.

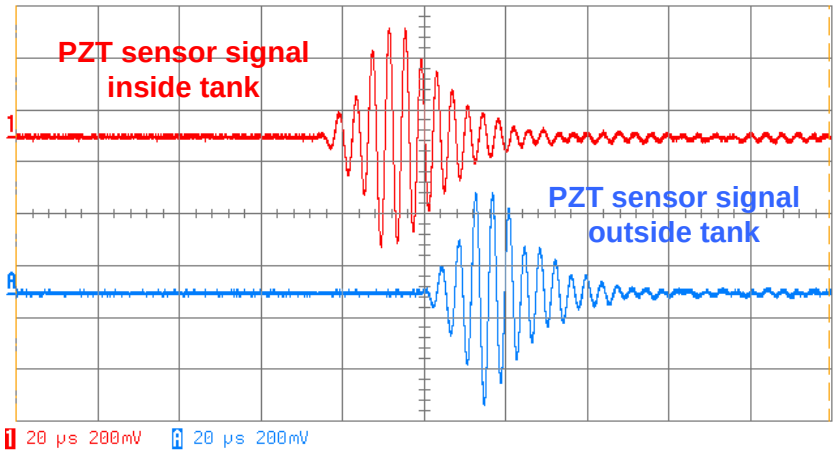

Figure 4-7
Sensor Amplified Signals PZT Sensor (a) Inside Tank; (b) Outside Tank

This test on one hand indicates that the tank might not be a good candidate to simulate a real transformer as its acoustic property might be significantly deviated from a transformer. On the hand, the test indicates that in real applications, the advantage of the optical sensors that they can be placed inside the transformer might be even more prominent than as shown in Test 1. From the result of Test 1, if the 20 dB attenuation of the wall of real transformers is considered, the SNR of the PZT sensor would be decreased to 2.2dB, because the noise which is induced mainly by the preamplifier remains no change, but the signal amplitude of the PZT sensor is decreased by 10 times.

Test 3: Head-to-Head Comparison of Optical and PZT Sensor Systems

This test is to compare the performances of the optical sensor and the PZT sensor at the same condition, i.e., when they see the same acoustic waves. In doing so, we measured and compared the SNRs of the two sensor systems when the PZT sensor and the optical sensor were placed at the same position. The Transimpedance amplifier used in the previous two tests was noisy. We found that the SNR of the optical sensor system was 6 dB worse than the PZT sensor system at such condition. However, to demonstrate the potential SNR of the optical sensor system, we used another transimpedance amplifier available at CPT which has a much smaller noise to replace the original transpedance amplifier. (It was not used in the bench-top system because it contains only 1 channel; while 4 channel amplifiers were required). The output signals of the PZT sensor and the optical sensor are shown in Figure 4-8. The peak-to-peak voltages are 4.2 and 2.3 V for PZT and optic sensors, respectively. The noise levels were calculated to be 8 and 6 mV respectively. Therefore, the PZT sensor system had SNR of 27.2 dB while the optical sensor system has a SNR of 25.8 dB. Even though the SNR of the optical sensor system was slightly smaller than

that of the PZT sensor system, the stronger acoustic waves inside the transformer would make up the difference. Further, we believe by choosing low-noise lasers and optimizing the electronic amplifier, the SNR performance of the optical sensor system can be significantly improved.

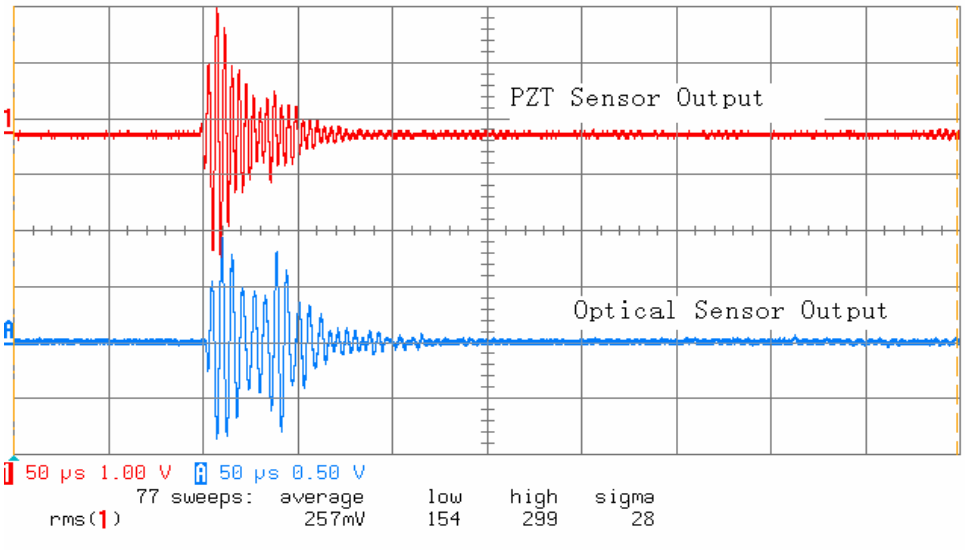

Figure 4-8
Output Signal of the PZT and Optical Sensors When They Are Placed at the Same Position in the Transformer

5
CONCLUSIONS

On-line monitoring of both hot-spots and partial discharge (PD) inside high-voltage transformers are an important step towards detecting imminent insulation problems and preventing catastrophic transformer failures. Fiber optic sensors are inherently advantageous for application within transformers because of their immunity to the strong electromagnetic interferences present inside the transformers – and due to the fact that they are an excellent dielectric – and hence can be safely inserted into the high electric fields in a transformer without compromising the insulation. In this research we developed and demonstrated in a laboratory an integrated fiber optical sensor system for both hot-spot and PD detections. This chapter summarizes the major conclusions obtained from the research.

Due to their capability of self-calibration and ease of dense multiplexing, fiber Bragg gratings (FBGs) were used for the multiplexed temperature measurement (hot-spot detection). The temperature was measured by the temperature-induced shift in Bragg wavelength. The gratings were fabricated with the phase-mask interferometer on hydrogen-loaded standard single mode fiber. Using a single phase mask, the FBG fabrication apparatus can write FBGs with arbitrary Bragg wavelengths.

We wrote nine FBGs, each with a different Bragg wavelength, in a single span of fiber for distributed temperature measurement. The signal was demodulated in the spectral domain with a Component Test System that can measure the reflection spectrum of the FBGs with high accuracy and resolution. The FBGs were annealed for better stability and then tested. The test results indicate that these FBG-based temperature sensors have uniform performance in terms of responsivity (~0.01 nm/°C) and measurement resolution (better than 0.1 °C).

We used diaphragm-based intrinsic Fabry-Perot (FP) interferometric fiber optic sensors for PD detections. With high sensitivity to acoustic waves and an all-glass structure, these sensors have been shown in our previous research extremely promising for the PD detections inside transformers. In this research, the fabrication process of these sensors was revolutionized by a new laser-fusion bonding method. Compared to the previous fabrication method, the laser-fusion bonding features more simplicity, better repeatability, and higher accuracy in controlling the FP cavity length. Moreover, the extremely high temperature in laser fusion bonding could generate a partial vacuum inside the FP cavity. The pressure of the air trapped inside the cavity is much smaller than the ambient air pressure. Therefore, the risk of the air discharge when it is placed inside the transformer is likely to be reduced. Confirmation of this fact in laboratory tests is included in the planned 2007 research.

The working point drift is always the most challenging problem in the signal demodulation of PD sensors. This problem was resolved by the two-laser quadrature method. Using two lasers

with quadrature wavelengths of the PD sensors, it is guaranteed that at any static background pressure at least one laser signal can provides sufficient sensitivity to acoustic waves. Compared to the tunable-filter-based demodulation used in our previous work, two-laser quadrature demodulation is more reliable, less costly and more (optical) power-efficient.

We multiplexed four PD sensors in our system. The FP cavity lengths of these sensors were controlled to be similar during fabrication. Therefore the sensors can share the same two laser sources during the quadrature demodulation. Each of the sensors together with the demodulation method was tested to be able to pick up the acoustic waves generated by an ultrasonic actuator in water.

Finally, we built a bench-top system at laboratory for principle demonstration. The system includes nine temperature sensors and four PD sensors. The system was tested and demonstrated in a large tank filled with water for both hot-spot and PD detections. We used a heater to locally heat the water to simulate the hot-spot and the ultrasonic actuator to simulate the PD-generated acoustic wave. The test and demonstration at laboratory were successful, showing the system is promising for the on-line monitoring of hot-spots and PD detections. We also compared the performances of our fiber optic PD sensors and commercial piezoelectric acoustic transceivers. The comparison indicates that the fiber optic sensor has comparable sensitivity to the piezoelectric sensor itself – and inherently improved sensitivity to detecting PD-generated acoustic waves in transformers because:

1. The fiber optic PD sensor can be placed inside the transformer where the acoustic wave is stronger.

2. The internal fiber optic sensor is not subjected to the attenuation through the tank walls.

6
SUGGESTION FOR FUTURE WORK

The results obtained in this research have demonstrated that the technology holds great promise for the on-line and multi-point detection of both hot-spots and partial discharge (PD) inside a high voltage transformer. In order to bring this technology to the level it can reliably monitor the thermal behavior and PD activities in real transformers, there are several tasks listed below that need to be completed.

- Develop more powerful signal-processing methods for detection weak PD activities. The PD activities inside a transformer sometime is so weak that it is not directly visible from the sensor output as it is hidden behind the noise. Therefore more advanced signal processing methods, such as those based on discrete wavelet transform, might be necessary to extract the signal from the noise.
- Investigate sensor package methods. Ideally, the sensors are permanently deployed into the transformers for on-line monitoring during the lifetime of the transformer. Good package of the sensors can protect the sensors from damage either during the deployment or in operation to extend their life of service.
- Investigate the long-term stability and reliability of the sensors. The performance of the sensors must be tested at laboratory before they can be placed inside real transformers. The long-term stability and reliability can be inferred from the relatively short-term laboratory test at the transformer oil environment with elevated temperature.
- Investigate the discharge possibility from the residual air trapped inside the FP cavity of the sensor. If it proves to be a concern, the PD sensors can be made inside a vacuum chamber so that no air will present inside the sensor.
- Investigate sensor deployment method. Ideally, the sensor system can be used in both the existing transformers in service and future transformer. Possible deployment methods together with appropriate sensor package need to be investigated for system deployment in currently in-use transformers.
- Translate the bench-top system into portable and user-friendly equipment.

Export Control Restrictions

Access to and use of EPRI Intellectual Property is granted with the specific understanding and requirement that responsibility for ensuring full compliance with all applicable U.S. and foreign export laws and regulations is being undertaken by you and your company. This includes an obligation to ensure that any individual receiving access hereunder who is not a U.S. citizen or permanent U.S. resident is permitted access under applicable U.S. and foreign export laws and regulations. In the event you are uncertain whether you or your company may lawfully obtain access to this EPRI Intellectual Property, you acknowledge that it is your obligation to consult with your company's legal counsel to determine whether this access is lawful. Although EPRI may make available on a case-by-case basis an informal assessment of the applicable U.S. export classification for specific EPRI Intellectual Property, you and your company acknowledge that this assessment is solely for informational purposes and not for reliance purposes. You and your company acknowledge that it is still the obligation of you and your company to make your own assessment of the applicable U.S. export classification and ensure compliance accordingly. You and your company understand and acknowledge your obligations to make a prompt report to EPRI and the appropriate authorities regarding any access to or use of EPRI Intellectual Property hereunder that may be in violation of applicable U.S. or foreign export laws or regulations.

The Electric Power Research Institute (EPRI)

The Electric Power Research Institute (EPRI), with major locations in Palo Alto, California, and Charlotte, North Carolina, was established in 1973 as an independent, nonprofit center for public interest energy and environmental research. EPRI brings together members, participants, the Institute's scientists and engineers, and other leading experts to work collaboratively on solutions to the challenges of electric power. These solutions span nearly every area of electricity generation, delivery, and use, including health, safety, and environment. EPRI's members represent over 90% of the electricity generated in the United States. International participation represents nearly 15% of EPRI's total research, development, and demonstration program.

Together…Shaping the Future of Electricity

Printed on recycled paper in the United States of America

1012342

Electric Power Research Institute
3420 Hillview Avenue, Palo Alto, California 94304-1338 • PO Box 10412, Palo Alto, California 94303-0813 • USA
800.313.3774 • 650.855.2121 • askepri@epri.com • www.epri.com